Journal of Computational Physics **175,** 269–301 (2002)
doi:10.1006/jcph.2001.6946, available online at http://www.idealibrary.com on IDEAL®

Shock-Capturing and Front-Tracking Methods for Granular Avalanches

Y. C. Tai,* S. Noelle,† J. M. N. T. Gray,‡ and K. Hutter*

*Institut für Mechanik, Technische Universität Darmstadt, 64289 Darmstadt, Germany; †Institut für Geometrie und Praktische Mathematik, RWTH Aachen, Templergraben 55, 52056 Aachen, Germany; and ‡Department of Mathematics, University of Manchester, Manchester M13 9PL, United Kingdom
E-mail: *tai@mechanik.tu-darmstadt.de, †noelle@igpm.rwth-aachen.de, ‡ngray@ma.man.ac.uk, *hutter@mechanik.tu-darmstadt.de

Received August 18, 2000; revised August 7, 2001

Shock formations are observed in granular avalanches when supercritical flow merges into a region of subcritical flow. In this paper we employ a shock-capturing numerical scheme for the one-dimensional Savage–Hutter theory of granular flow to describe this phenomenon. A Lagrangian moving mesh scheme applied to the nonconservative form of the equations reproduces smooth solutions of these free boundary problems very well, but fails when shocks are formed. A nonoscillatory central (NOC) difference scheme with TVD limiter or WENO cell reconstruction for the conservative equations is therefore introduced. For the avalanche free boundary problems it must be combined with a front-tracking method, developed here, to properly describe the margin evolution. It is found that this NOC scheme combined with the front-tracking module reproduces both the shock wave and the smooth solution accurately. A piecewise quadratic WENO reconstruction improves the smoothness of the solution near local extrema. The schemes are checked against exact solutions for (1) an upward moving shock wave, (2) the motion of a parabolic cap down an inclined plane, and (3) the motion of a parabolic cap down a curved slope ending in a flat run-out region, where a shock is formed as the avalanche comes to a halt.

Key Words: granular avalanche; shock-capturing; nonoscillatory central scheme; free moving boundary; front-tracking.

1. INTRODUCTION

Snow avalanches, landslides, rock falls, and debris flows are extremely dangerous and destructive natural phenomena, and their occurrence has increased during the past few decades. Their human impact has become so significant that the United Nations declared 1990–2000 the International Decade for Natural Disaster Reduction. Research on the protection of

0021-9991/02 $35.00

habitants from floods, debris flows, and avalanches is under way worldwide, and many institutions focus on the numerical prediction of such flows under ideal as well as realistic conditions.

One of the models that has become popular in recent years is the Savage–Hutter (SH) avalanche theory for granular materials [33, 34]. In the past decade numerical techniques were developed to solve the SH-governing differential equations for typical moving boundary value problems [6–10, 13, 14, 16, 19, 33, 34, 41]. These techniques are based on a Lagrangian moving mesh finite-difference scheme in which the granular material is divided into quadrilateral cells (2D) or triangular prisms with flat tops (3D). Exact similarity solutions of the SH equations were constructed in spatially one-dimensional chute flows [32, 33, 35] and for two-dimensional unconfined flows [12, 15]. In the case of chute flows it was shown that the solutions obtained by the Lagrangian integration procedure approximate the exact parabolic similarity solution very accurately, and these theoretical and numerical results are in good agreement with experimental avalanche data. Similar agreement between theoretical, numerical, and experimental data was also obtained for the two-dimensional flow configurations (cf. above references). In these Lagrangian schemes explicit, artificial numerical diffusion was incorporated to maintain stability. In doing so the quality of resolution deteriorates. In fact, the adequacy of these numerical solutions can be challenged because of uncontrolled spreading due to this diffusion. It was also observed that the Lagrangian schemes lose their stability (or else unjustified artificial diffusion must be applied) whenever internal shocks are formed. This appears to occur whenever the avalanche moves from an extending to a contracting flow configuration. These shocks are travelling waves which form bumps with steep gradients on the free surface, which is thicker on the downslope side. It is therefore natural to develop conservative, high-resolution, shock-capturing numerical techniques that are able to resolve the steep surface gradients and identify the shocks often observed in experiments but not captured by the Lagrangian finite difference scheme.

The development of high-resolution shock-capturing schemes has a long history which we cannot even sketch here (see, e.g., the classical references [3, 11, 40, 42] or the recent textbooks [4, 20, 25, 39]. The most common approach is to first develop a one-dimensional, total-variation-diminishing (TVD) upwind scheme for a scalar conservation law and then apply it to systems using one-dimensional characteristic decompositions or approximate Riemann solvers. Upwind schemes have been used very successfully for gas dynamical calculations, where the Riemann problem can be solved exactly and many approximate Riemann solvers are available. For more complicated systems like the granular flow model considered here characteristic decompositions are often not available, and the Riemann problem cannot be solved analytically. Therefore we have chosen an alternative approach to high-resolution shock-capturing, namely the recent nonoscillatory central (NOC) schemes first introduced by Nessyahu and Tadmor [30]. While upwind schemes are higher order extensions of the classical Godunov scheme, central schemes build upon the (also classical) Lax–Friedrichs scheme [23]. This scheme avoids characteristic decompositions and Riemann solvers by the use of a staggered grid. When used together with piecewise constant spatial reconstructions, the Lax–Friedrichs scheme is more diffusive than Godunov's scheme. However, when one combines the scheme with TVD-type piecewise linear reconstructions, it becomes competitive with the upwind schemes. Recently, central schemes have been extended in many directions; see, e.g., [1, 2, 18, 27] for multidimensional extensions, [31] for an adaptive staggered scheme, [26, 28] for third- and higher order schemes, and

[21, 22] for central schemes on nonstaggered grids, which are precisely at the borderline of central and upwind schemes.

Here we adapt the second-order NOC scheme of Nessyahu and Tadmor to include an earth pressure coefficient, which has a jump discontinuity as the flow travels from an expanding into a contracting region, and to treat the source term, which is due to the spatially varying topography and the gravitational force. The resulting scheme works well both in smooth regions and at shocks, which are captured within two mesh cells and without any oscillations.

Besides the formation of shock fronts in the interior, avalanches may have a vacuum front at their margins. Similarly as for the equations of gas dynamics, the hyperbolic system degenerates at the vacuum state. Many shock-capturing upwind schemes produce negative heights at these points and subsequently break down or become completely unstable. While our NOC scheme is remarkably stable at the margins, it does not capture the vacuum front as well as the Lagrangian moving mesh scheme. To overcome this imperfection, we augmented the NOC scheme with an algorithm that tracks the vacuum front. The combined front-tracking, nonoscillatory central scheme is accurate and robust both at shocks and at the margins of the granular avalanche.

The ensuing analysis commences in Section 2 with the presentation of the governing SH equations in conservative and nonconservative form; then the jump conditions of mass and momentum at singular surfaces are stated and the solution to a single shock wave (a hydraulic jump) are presented. Section 2 closes with the construction of exact similarity solutions of a parabolic heap moving down a rough incline. Section 3 introduces the numerical techniques. At first the Lagrangian integration technique is described; it is followed by the presentation of the nonoscillatory central scheme. In Section 4 we augment the NOC scheme (which uses a fixed Eulerian grid) with a Lagrangian-type front-tracking method in the marginal cells. Section 5 elaborates on numerical results. The travelling shock wave cannot be handled by the Lagrangian method, but the NOC scheme can handle it with very little diffusion across the shock. On the other hand, the parabolic similarity solution is well produced by the Lagrangian integration technique, but much less accurately by the NOC schemes unless Lagrangian front-tracking is introduced for the marginal cells. It is also shown that the NOC scheme with piecewise linear spatial reconstructions applying standard TVD-type slope limiters exhibits some oscillations near smooth local maxima. We remove these oscillations by incorporating a piecewise quadratic weighted essentially nonoscillatory (WENO) reconstruction into our scheme. Our final numerical experiment combines all the difficulties treated in the paper: an avalanche with a vacuum front at the margins expands as it flows downhill and contracts as it hits the flat runout (so the earth pressure coefficient changes discontinuously at the transition point). As the avalanche comes to a halt at the bottom, a shock wave develops and propagates upslope. Our NOC front-tracking scheme handles this challenging flow very satisfactorily. Section 6 presents conclusions and gives an outlook for further work.

2. GOVERNING EQUATIONS

A detailed derivation of the Savage–Hutter theory has been given in [33, 34]. Here we confine ourselves to a brief description. Although cohesionless granular materials exhibit dilatancy effects numerous experiments have confirmed that during rapid dense flow it is reasonable to assume that the avalanche is incompressible with constant uniform density ρ_0.

During flow a body behaves as a Mohr–Coulomb plastic material at yield. As the avalanche slides over the rigid basal topography a Coulomb dry friction force resists the motion. The basal shear stress is therefore equal to the normal basal pressure multiplied by a coefficient of friction $\tan\delta$, where δ is termed the basal friction angle [19]. Scaling analysis isolates the physically significant terms in the governing equations and identifies those terms that can be neglected. Plane flow configurations are our focus in this paper, so depth integration reduces the theory to one spatial dimension. The leading order, dimensionless, depth-integrated equations for the local thickness of the avalanche h and the momentum hu (u is the downslope velocity) reduce to

$$\frac{\partial h}{\partial t} + \frac{\partial}{\partial x}(hu) = 0, \tag{1}$$

$$\frac{\partial (hu)}{\partial t} + \frac{\partial}{\partial x}(hu^2 + \beta_x h^2/2) = h s_x \tag{2}$$

with net driving force

$$s_x = \sin\zeta - \operatorname{sgn}(u)\tan\delta(\cos\zeta + \lambda\kappa u^2) - \varepsilon\cos\zeta\frac{\partial z^b}{\partial x}, \tag{3}$$

where x is the arc length measured along the avalanche track, z^b denotes the height of the basal topography relative to the track (usually $z^b = 0$ in one spatial dimension), and ζ and $\lambda\kappa$ are the local slope inclination angle and curvature of the track, respectively. The term $\operatorname{sgn}(u)$ selects the orientation of the dry Coulomb drag friction, and $\varepsilon \ll 1$ is the aspect ratio of a typical thickness and length of the avalanche. Note that Eqs. (1) and (2) are written in conservative form [8], while in the original SH theory the smoothness assumption allows the momentum balance equation to transform to an evolution equation for the velocity, viz.,

$$\frac{du}{dt} = s_x - \beta_x\frac{\partial h}{\partial x} - \frac{1}{2}h\frac{\partial \beta_x}{\partial x}. \tag{4}$$

The factor β_x is defined as $\beta_x = \varepsilon\cos\zeta K_x$ and the earth pressure coefficient K_x is given by the ad hoc assumption

$$K_x = \begin{cases} K_{x_{act}} & \text{for } \partial u/\partial x > 0, \\ K_{x_{pass}} & \text{for } \partial u/\partial x < 0, \end{cases} \tag{5}$$

with

$$K_{x_{act/pass}} = 2(1 \mp \sqrt{1 - \cos^2\phi/\cos^2\delta})\sec^2\phi - 1, \tag{6}$$

and ϕ is the internal friction angle of the granular material. Note that the values of the earth pressure coefficient K_x are based on the postulation of Mohr–Coulomb plastic behaviour for the cohesionless yield on the basal sliding surface; see Savage and Hutter [33, 34] for details. In this theory the earth pressure coefficient K_x is assumed to be a function of the velocity gradient; i.e., $K_x = K_x(\partial u/\partial x)$.

The governing equations look like the shallow-water equations, but because of the jump in the earth pressure coefficients $K_{x_{act/pass}}$, the source term s_x, and the free boundary at the front and rear margins, it becomes much more complicated to develop an appropriate

numerical scheme to describe the flow. The original Lagrange finite-difference scheme [33] is implemented for the equation Systems (1) and (4) in Lagrangian form, with primitive variables h and u. The shock-capturing scheme developed here is applied to the system in conservative form (1) and (2), where the conserved quantities are the avalanche thickness h and the depth-integrated momentum $m = hu$.

In vector notation, Eqs. (1) and (2) take the form

$$\boldsymbol{w}_t + \boldsymbol{f}_x = \boldsymbol{s}, \tag{7}$$

where

$$\boldsymbol{w} = \begin{pmatrix} h \\ m \end{pmatrix}, \quad \boldsymbol{f} = \begin{pmatrix} m \\ m^2/h + \beta_x h^2/2 \end{pmatrix}, \quad \text{and} \quad \boldsymbol{s} = \begin{pmatrix} 0 \\ hs_x \end{pmatrix}. \tag{8}$$

This form is more convenient for mathematical analysis than that of (1) and (2).

2.1. Jump Condition and Travelling Wave

The Savage–Hutter theory can be used to model the upslope propagating travelling shock wave observed in experiments [5, 7] by introducing the jump conditions (see Fig. 1) of the balance equations (1) and (2) for mass and momentum,

$$[\![h(u - V_n)]\!] = 0, \tag{9}$$

$$\left[\!\left[hu(u - V_n) + \frac{1}{2}\beta_x h^2\right]\!\right] = 0, \tag{10}$$

where V_n is the normal speed of the singular surface. Let us suppose that $[\![\beta_x]\!] = 0$ (for example, this is always satisfied if $\phi = \delta$; i.e., $K_{x_{act}} = K_{x_{pass}}$). Substituting (9) into (10) (i.e., eliminating V_n) yields the following relation between the depth ratio, $H := h^-/h^+$, and the velocity difference:

$$(u^+ - u^-)^2 = \beta_x h^- \frac{H+1}{2}\left(\frac{H-1}{H}\right)^2. \tag{11}$$

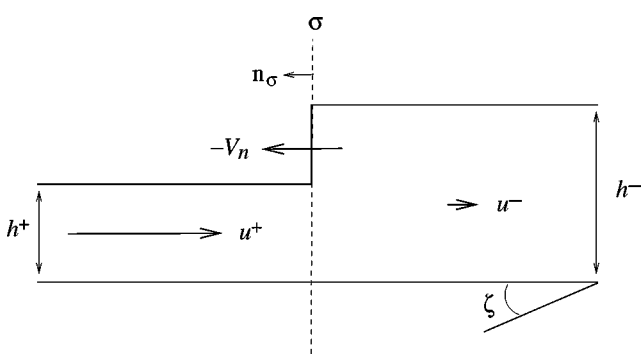

FIG. 1. The plane travelling shock wave can be interpreted as a jump in thickness and velocity separating the body of the avalanche into two parts on a plane with inclined angle ζ. h^+ and h^- are the thicknesses of both sides and u^+ and u^- are the velocities, respectively, whereas this jump travels with velocity V_n up slopes.

For an upslope travelling shock wave with travelling wave speed V_n and corresponding depth ratio H, the factor β_x is a function of material and topographic parameters, ϕ, δ, and ζ, which are given by the selected material and topography. Provided that the depths before and after the shock, h^+ and h^-, are known (they can be determined by experiment) and the downslope velocity is also given (it is normally equal to zero), the upslope velocity can be determined by using (11):

$$u^+ = u^- \pm \frac{H-1}{H}\left[\beta_x h^- \frac{H+1}{2}\right]^{1/2}. \tag{12}$$

Note that the term under the square root is positive for all positive H. If $H = 1$ then $u^+ = u^-$, which indicates that no shock wave (discontinuity) takes place. Thus, velocity jumps and depth jumps occur together.

By inspection of the mass balance equation (9), the velocity of the shock is given by

$$V_n = \frac{Hu^- - u^+}{H-1} = u^- \mp \left[\beta_x h^- \frac{H+1}{2H^2}\right]^{1/2}. \tag{13}$$

Note that as h^+ tends to $h = h^-$, u^+ tends to $u = u^-$ and

$$V_n \to u \mp [\beta_x h]^{1/2}, \tag{14}$$

so we have recovered the characteristic speeds of the shallow-water equations. Now we apply Lax shock inequalities [24] to single out the physically relevant branches of the shock curves: for the first family, with characteristic speed $u - \sqrt{\beta_x h}$, we require that

$$u^+ - [\beta_x h^+]^{1/2} > V_n = u^- - \left[\beta_x h^- \frac{H+1}{2H^2}\right]^{1/2} > u^- - [\beta_x h^-]^{1/2},$$

which implies $H > 1$ (recall that the upslope state "+" lies to the left of the shock). Analogously, for the second family, with characteristic speed $u + \sqrt{\beta_x h}$, we obtain $H < 1$. For example, an upward jump ($h^+ < h^-$) can only be carried by a shock of the first family, and in this case $u^+ > u^- > V_n$, so particles which cross the shock are condensed and slow down.

2.2. Similarity Solution

Consider the motion of a finite mass of granular material along a flat plane, i.e. ζ is constant and $\lambda\kappa = 0$ in (3). In [33] one particular similarity solution to a moving boundary problem of finite mass was derived; this solution is now generalised (see [36]). To this end we introduce a moving coordinate system with velocity

$$u_0(t) = u_0(0) + \int_0^t (\sin\zeta - \tan\delta\, \cos\zeta)\, dt \tag{15}$$

on a plane with inclination angle ζ. This velocity is due to the net driving force s_x in (3), where we assume that the velocity is positive for positive times; i.e., $\mathrm{sgn}(u) = 1$. The relative velocity $\breve{u}$ in the moving coordinate system is then given by

$$\breve{u} = u - u_0(t). \tag{16}$$

A symmetric bulk is considered and the origin of the moving coordinate system is selected to lie at the centre where the surface gradient, $\partial h/\partial x$, is zero. To keep the symmetric depth profile during the motion the relative velocity is further assumed to be skew–symmetric, $\breve{u}(\xi, t) = -\breve{u}(-\xi, t)$, where

$$\xi = x - \int_0^t u_0(t')\, dt' \tag{17}$$

indicates the distance from the origin in the moving coordinates. Provided that $g(t)$ is the distance from the coordinate origin to the margin at time t, the physical domain occupied by the granular mass can be mapped from $[-g(t), g(t)]$ to the fixed domain $[-1, 1]$ by

$$\eta = \frac{1}{g(t)}\left\{x - \int_0^t u_0(t')\, dt'\right\}, \quad \text{where } \eta \in [-1, 1]. \tag{18}$$

With this coordinate mapping, $(x, t) \to (\eta, \tau)$, the model equations (1) and (2) reduce to

$$\frac{\partial h}{\partial t} - \eta\frac{g'}{g}\frac{\partial h}{\partial \eta} + \frac{1}{g}\frac{\partial}{\partial \eta}(h\breve{u}) = 0, \tag{19}$$

$$\frac{\partial \breve{u}}{\partial t} - \eta\frac{g'}{g}\frac{\partial \breve{u}}{\partial \eta} + \frac{1}{g}\left(\breve{u}\frac{\partial \breve{u}}{\partial \eta} + \beta_x\frac{\partial h}{\partial \eta}\right) = 0, \tag{20}$$

where the τ is again replaced by t and we have used $g' = dg/dt = -u_0/\eta$.

Now we assume that $\breve{u}(\eta, t)$ varies linearly in η. Since the margins move with relative speeds $\pm g'(t)$, this yields $\breve{u}(\eta, t) = \eta g'(t)$. Now the evolution equations (19) and (20) reduce to

$$\frac{\partial h}{\partial t} + \frac{g'}{g}h = 0, \tag{21}$$

$$\eta g'' + \frac{\beta_x}{g}\frac{\partial h}{\partial \eta} = 0, \tag{22}$$

where $g'' = d^2g/dt^2$. Integrating (22) subject to the boundary condition either $h(\eta = 1) = 0$ or $h(\eta = -1) = 0$, it follows that the thickness is described by

$$h(\eta, t) = \frac{g(t)g''(t)}{2\beta_x}(1 - \eta^2). \tag{23}$$

This implies that the avalanche body keeps a parabolic thickness distribution during the motion. With the thickness distribution (23) one can easily obtain the total mass M to be

$$M = \int_{\xi_f}^{\xi_{Ft}} h(\xi, t)\, d\xi = \int_{-1}^{1} h(\eta, t)g(t)\, d\eta = \frac{2}{3}\frac{g''g^2}{\beta_x}. \tag{24}$$

Since mass is conserved,

$$0 = \frac{d}{dt}M = \frac{2g}{3\beta_x}(2g'g'' + gg'''). \tag{25}$$

This relation can also be derived directly from the mass balance equation (21).

Changing the independent variable t to $g(t)$ and letting $p(t) = g'(t)$, Eq. (24) can be written as

$$p\frac{dp}{dg} = \frac{K}{g^2}, \tag{26}$$

where $3\beta_x M = 2K$. The similarity solution is then obtained by solving (26) with initial conditions, $g(0) = g_0$ and $p(0) = p_0$:

$$p^2(t) = 2K\left(\frac{1}{g_0} - \frac{1}{g(t)}\right) + p_0^2. \tag{27}$$

With the definition $\alpha_g = \frac{2K}{g_0}$, $\beta_g = p_0^2$, and $G = (\alpha_g + \beta_g)g$ it follows that

$$\frac{\sqrt{G}G'}{\sqrt{G - 2K}} = (\alpha_g + \beta_g)^{3/2}. \tag{28}$$

We now use the relation

$$\frac{d}{dG}[\sqrt{G}\sqrt{G - 2K} + 2K\ln(\sqrt{G} + \sqrt{G - 2K})] = \frac{\sqrt{G}}{\sqrt{G - 2K}}$$

and integrate Eq. (28) to yield

$$\begin{aligned}&\sqrt{G}\sqrt{G - 2K} + 2K\ln(\sqrt{G} + \sqrt{G - 2K})\\ &\quad -[\sqrt{G}\sqrt{G - 2K} + 2K\ln(\sqrt{G} + \sqrt{G - 2K})]_{t=0} = (\alpha_g + \beta_g)^{3/2}t.\end{aligned} \tag{29}$$

With $g_0 = 1$, $p_0 = 0$ we obtain the Savage–Hutter solution [33]

$$\sqrt{g}\sqrt{g - 1} + \ln(\sqrt{g} + \sqrt{g - 1}) = \sqrt{2K}t, \tag{30}$$

for which $g(t) > 1$. Both (29) and (30) are implicit evolution equations for $g(t)$. Once $g(t)$ is deduced, with the presumption $\breve{u}(\eta, t) = \eta g'(t)$, the complete solution is then given by (23) and (27),

$$\breve{u}(\eta, t) = \eta\left\{2K\left(\frac{1}{g_0} - \frac{1}{g(t)}\right) + p_0^2\right\}^{1/2}, \quad h(\eta, t) = \frac{3M}{4g(t)}(1 - \eta^2), \tag{31}$$

where η is defined in (18). In the present similarity solution it is presumed that $u/|u| = 1$, which means that $u > 0$ for all $t \geq 0$. From (16) and the presumption that $\breve{u}(\eta, t) = \eta g'(t)$ it follows that

$$u(t) = u_0(t) + \breve{u}(t) > 0 \Rightarrow g'(t) < u_0(t), \quad \text{for all } t \geq 0. \tag{32}$$

It is very important to verify that the velocity is consistent with condition (32) to keep the parabolic similarity solution valid. The generalisation (29) of (30) was needed to have exact solutions with nonvanishing initial velocities (for further details see [36]).

3. NUMERICAL SCHEME

The numerical schemes employed in this paper are designed to explicitly solve the system of equations in 1D and we here introduce a Lagrangian algorithm and an Eulerian shock-capturing NOC scheme.

In the Lagrangian technique [33, 34] the avalanche body is divided into several cells. The purpose is to find the velocity of the cell boundaries in order to determine the cell boundary locations for each time step, so it is a moving-grid method, whereas the NOC scheme is built on a stationary uniform grid and gives a high resolution of the shock solutions without any spurious oscillations near a discontinuity.

In the Lagrangian method the value of the depth h_j^n is defined as the volume average within the jth cell for time t^n, which is bounded by $b_{j-1}(t)$ and $b_j(t)$, and the boundary $b_j(t)$ moves with the velocity u_j. Whilst, in the NOC scheme the value of the discretised variable U_j^n, $U = h, m$ is defined on the mesh as the volume average within the jth mesh cell centred at position x_j for time t^n, where the jth cell is bounded by $x_{j+1/2}$ and $x_{j-1/2}$.

3.1. Lagrangian Method

In the Lagrangian method [33, 34] the avalanche body is divided into N material cells, where $x = b_{j-1}(t)$ and $x = b_j(t)$ denote the boundaries of the cell j at time t; see Fig. 2. These boundaries move with the avalanche velocity; i.e.,

$$\frac{d}{dt} b_j(t) = u_j(t) = u(b_j(t), t).$$

Integrating the mass balance equation (1) over the cell yields

$$\int_{b_{j-1}}^{b_j} \left\{ \frac{\partial h}{\partial t} + \frac{\partial}{\partial x}(hu) \right\} dx = \frac{d}{dt} \int_{b_{j-1}}^{b_j} h \, dx = 0 \Rightarrow \frac{d}{dt} V_{cell_j} = 0 \tag{33}$$

and implies that the volume (mass) of the cell is conserved during the motion. Because of this, the mean height of the jth cell can be determined by

$$h_j^n = \frac{V_{cell_j}}{b_j^n - b_{j-1}^n}. \tag{34}$$

The computations proceed as follows. It is assumed that b_j^n, h_j^n, and $u_j^{n+1/2}$ are given as initial values and the new location of the cell boundary b_j^{n+1} after an elapsed time Δt is

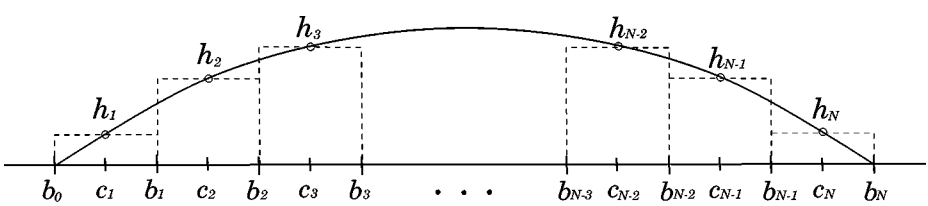

FIG. 2. The avalanche body is divided into N elements with average depth h_j, where c_j is the centre of the jth element.

given by

$$b_j^{n+1} = b_j^n + \Delta t u_j^{n+1/2}. \tag{35}$$

Note that here the velocity u_j indicates the boundary velocity of b_j. The momentum balance (4) allows the velocity of the cell boundary at time $t^{n+1/2}$ to be determined,

$$u_j^{n+1/2} = u_j^{n-1/2} + \Delta t \left\{ s_j^n - \varepsilon \cos\zeta_j (K_x)_j^n \left(\frac{\partial h}{\partial x}\right)_j^n - \varepsilon \frac{h_{j+1/2}^n}{2} \left(\frac{\partial(\cos\zeta K_x)}{\partial x}\right)_j^n \right\}. \tag{36}$$

The net driving acceleration s_j^n as given by (3) is

$$s_j^n = \sin\zeta_j - \operatorname{sgn}\left(u_j^{n-1/2}\right) \tan\delta \left\{ \cos\zeta_j + \lambda\kappa_j \left(u_j^{n-1/2}\right)^2 \right\} - \varepsilon \cos\zeta_j \left(\frac{\partial z^b}{\partial x}\right)_j, \tag{37}$$

where ζ_j represents the local inclination angle, κ_j is the local curvature, and z^b denotes the local basal topography. Note that the last term at the right-hand side of (36) contains the gradient of the earth pressure coefficient, which is neglected in the numerical scheme of Savage and Hutter [33, 34].

The earth pressure coefficient K_x is determined by the ad hoc definition

$$(K_x)_j^n = \begin{cases} K_{x_{act}}, & \text{for } u_{j+1}^{n-1/2} \geq u_j^{n-1/2}, \\ K_{x_{pass}}, & \text{for } u_{j+1}^{n-1/2} < u_j^{n-1/2} \end{cases} \tag{38}$$

in [33, 34]. The surface (depth) gradients in (36) are determined by the depths of the adjacent elements

$$\left(\frac{\partial h}{\partial x}\right)_j^n = \frac{\left(h_{j+1}^n - h_j^n\right)}{c_{j+1}^n - c_j^n} = \frac{2\left(h_{j+1}^n - h_j^n\right)}{b_{j+1}^n - b_{j-1}^n}, \tag{39}$$

where c_j^n represents the centre of the jth cell, $c_j^n = (b_j^n + b_{j-1}^n)/2$, at time $t = t^n$; see Fig. 2. The height at the cell boundary, $h_{j+1/2}$, is given by their mean values in adjacent cells, $h_{j+1/2} = \frac{1}{2}(h_j + h_{j+1})$, and the gradient of the earth pressure coefficient is

$$\left(\frac{\partial(\cos\zeta K_x)}{\partial x}\right)_j^n = \frac{\cos\zeta_{j+1}(K_x)_{j+1}^n - \cos\zeta_j (K_x)_j^n}{c_{j+1}^n - c_j^n}. \tag{40}$$

However, while this method is excellent for classical smooth solutions, it loses numerical stability if shocks develop. Shocks are initiated when the avalanche velocity is faster than its characteristic speed and the avalanche front reaches the base of the slope or a solid wall. Many detailed investigations about granular shocks were made by Gray and Hutter [5], in which the shock waves are considered to be an important property in the granular flows. To avoid the numerical instability caused by the shocks, an artificial viscosity term $\mu\partial^2 u/\partial x^2$ is introduced and added to the right-hand side of (37) for numerical stability, e.g., [14, 33, 34], where the artificial viscosity μ was found to have values between 0.01 and 0.03.

3.2. NOC Scheme

The nonoscillatory central difference scheme of Nessyahu and Tadmor [30] is a second-order-accurate extension of the classical Lax–Friedrichs scheme [23]. Let us briefly review the NOC scheme:

We consider the Savage–Hutter equations in the conservative form (7), (8) with $\boldsymbol{w} = (h, m)^T$ as basic variables. Let $\bar{\mathbf{w}}_j^n$ denote the cell average over the interval $[x_{j-1/2}, x_{j+1/2}]$ at time t^n, and let

$$\bar{\mathbf{w}}(x, t^n) = \bar{\mathbf{w}}_j^n + \frac{x - x_j}{\Delta x}\bar{\mathbf{w}}_j' \tag{41}$$

be a piecewise linear reconstruction over the cell, where $\bar{\mathbf{w}}_j'$ denotes the cell mean derivative determined by a TVD limiter [25] or a central WENO cell reconstruction [26]. The main conceptual difference between the NOC schemes and standard, upwind, finite difference schemes is the use of a staggered grid. At time $t^{n+1} = t^n + \Delta t$, the cell averages $\bar{\mathbf{w}}_{j+1/2}^{n+1}$ are evaluated over the intervals $[x_j, x_{j+1}]$; see Fig. 3. As a consequence, the boundaries of the cells at the new time level are the *centers* of the cells at the old time level, namely the points x_j and x_{j+1}. At these points, the piecewise polynomial reconstruction (41) of the cell averages at the old time level t^n is smooth, and it remains so for $t < t^{n+1}$ under an appropriate restriction of the timestep (see (49) below). Therefore, the flux across the boundaries of the cells at the new time level may be evaluated by Taylor extrapolations using the differential equation and standard quadrature rules. Here we use the midpoint rule in time to achieve second-order accuracy. The resulting update takes the form

$$\bar{\mathbf{w}}_{j+1/2}^{n+1} = \frac{1}{2}\left(\bar{\mathbf{w}}_{j+1/4}^n + \bar{\mathbf{w}}_{j+3/4}^n\right) - \frac{\Delta t}{\Delta x}\left(\mathbf{f}_{j+1}^{n+1/2} - \mathbf{f}_j^{n+1/2}\right) + \frac{\Delta t}{2}\left(\mathbf{s}_{j+1/4}^{n+1/2} + \mathbf{s}_{j+3/4}^{n+1/2}\right), \tag{42}$$

as illustrated in Fig. 3b. The values of $\bar{\mathbf{w}}_{j+1/4}^n$ and $\bar{\mathbf{w}}_{j+3/4}^n$ are determined by the reconstruction (41) over the jth and $(j+1)$th cells; i.e.,

$$\bar{\mathbf{w}}_{j+1/4}^n = \bar{\mathbf{w}}_j^n + \frac{1}{4}\bar{\mathbf{w}}_j', \quad \bar{\mathbf{w}}_{j+3/4}^n = \bar{\mathbf{w}}_{j+1}^n - \frac{1}{4}\bar{\mathbf{w}}_{j+1}'. \tag{43}$$

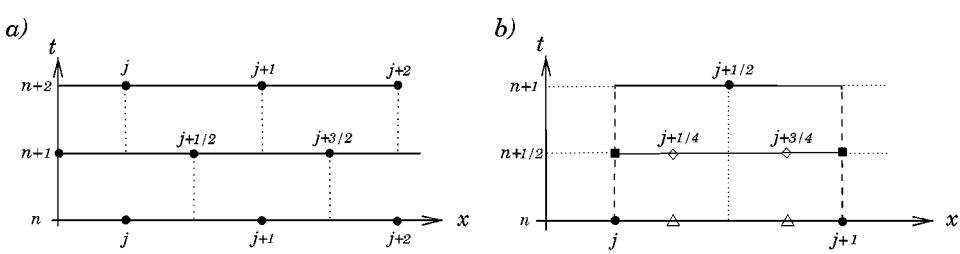

FIG. 3. Diagram of NOC-S scheme. (a) Grid points computed by the NOC-S method. (b) NOC-S computational diagram, where ● indicates the grid points at time level n and $n+1$, ■ represents the quadrature points for the fluxes $\mathbf{f}$ across the cell boundaries, ◇ shows the quadrature points for the source terms $\mathbf{s}$, and Δ indicates those for the staggered cell averages at the original time t^n.

The transport flux $\mathbf{f}$ at the quadrature points $(x_j,\ t^{n+1/2})$ and $(x_{j+1},\ t^{n+1/2})$ is approximated by Taylor extrapolation in time,

$$\mathbf{f}_j^{n+1/2} = \mathbf{f}\big(\bar{\mathbf{w}}_j^{n+1/2}\big), \quad \bar{\mathbf{w}}_j^{n+1/2} = \bar{\mathbf{w}}_j^n + \frac{\Delta t}{2}(\partial\bar{\mathbf{w}}/\partial t)_j^n, \tag{44}$$

and similarly, the source terms $\mathbf{s}$ at the quadrature points $(x_{j+1/4},\ t^{n+1/2})$ and $(x_{j+3/4},\ t^{n+1/2})$ are approximated by space–time Taylor extrapolation

$$\begin{aligned}
&\mathbf{s}_{j+1/4}^{n+1/2} = \mathbf{s}\big(\bar{\mathbf{w}}_{j+1/4}^{n+1/2}\big), \quad \bar{\mathbf{w}}_{j+1/4}^{n+1/2} = \bar{\mathbf{w}}_j^n + \frac{\Delta t}{2}(\partial\bar{\mathbf{w}}/\partial t)_j^n + \frac{1}{4}\bar{\mathbf{w}}_j', \\
&\mathbf{s}_{j+3/4}^{n+1/2} = s\big(\bar{\mathbf{w}}_{j+3/4}^{n+1/2}\big), \quad \bar{\mathbf{w}}_{j+3/4}^{n+1/2} = \bar{\mathbf{w}}_{j+1}^n + \frac{\Delta t}{2}(\partial\bar{\mathbf{w}}/\partial t)_{j+1}^n - \frac{1}{4}\bar{\mathbf{w}}_{j+1}'.
\end{aligned} \tag{45}$$

The temporal derivative $(\partial\bar{\mathbf{w}}/\partial t)_j^n$ in (44) and (45) is determined by using (7),

$$(\partial\bar{\mathbf{w}}/\partial t)_j^n = -(\partial\mathbf{f}/\partial x)_j^n + \mathbf{s}_j^n = -\mathbf{A}_j\bar{\mathbf{w}}_j'/\Delta x + \mathbf{s}_j^n, \tag{46}$$

where

$$(\partial\mathbf{f}/\partial x)_j^n = (\mathbf{A})_j^n(\partial\mathbf{w}/\partial x)_j^n, \quad \mathbf{A} = \partial\mathbf{f}/\partial\mathbf{w} = \begin{pmatrix} 0 & 1 \\ -\frac{m^2}{h^2} + \beta_x h & \frac{2m}{h} \end{pmatrix} \tag{47}$$

and $\mathbf{A}$ is the Jacobian of $\mathbf{f}$. Alternatively, one may also use the Jacobian-free approach of Nessyahu and Tadmor [30] and set

$$(\partial\mathbf{f}/\partial x)_j^n = \mathbf{f}'_j/\Delta x,$$

where the cell mean derivative $\mathbf{f}'$ of the flux is again determined by a TVD limiter. Let a^{max} be the maximum wave speed,

$$a^{max} = \max_{all\ j}(|u_j| + \sqrt{\beta_j h_j}), \quad u_j = m_j/h_j \quad \text{for } h_j \neq 0. \tag{48}$$

The CFL condition

$$\frac{\Delta t}{\Delta x}|a^{max}| < \frac{1}{2}, \quad \text{for all } j \tag{49}$$

is needed to guarantee that the solution remains smooth at the space–time quadrature points, so that the Taylor expansions (44) and (45) are justified.

Note that the NOC scheme (41)–(49) completely avoids the expensive Riemann solvers used in standard upwind schemes on nonstaggered grids. The resulting staggered schemes are easy to code and computationally efficient and can be applied to general systems of conservation laws, where the solution of the Riemann problem (i.e., the initial value problem with piecewise constant data) may be complicated or even impossible.

4. FRONT-TRACKING METHOD

In many applications, the region covered by the granular material has a finite extension and is limited by a free boundary which moves with the flow velocity. Outside this region, there is a vacuum, so the avalanche height h and momentum m are zero, and the velocity $u = m/h$ is not well defined. The Lagrangian method handles this situation automatically, since the computational domain moves with the material flow. The NOC scheme discretizes the differential equations on a stationary uniform mesh. Note that in general the margin points x_{Ft}^n (the front margin) and x_{Tl}^n (the tail margin) lie between grid points, so that it is impossible to point out the margin locations without extra treatment. Furthermore, it is not straightforward to determine the proper cell reconstructions over the margin cells. Figure 4 illustrates an example of depth reconstruction over the front margin cell determined by various TVD limiters. Here and in the following we suppose that at time t_n, the front margin lies in the fth cell, $x_{f-1/2} < x_{Ft}^n \le x_{f+1/2}$, and the tail margin in the tth cell, $x_{t-1/2} \le x_{Tl}^n < x_{t+1/2}$.

Since our quadrature rule for the fluxes (44), (46), (47) uses a Taylor expansion of the solution, different limiters will lead to different values of the integrals of the fluxes across $x_f \times [t_n, t_{n+1}]$ and $x_t \times [t_n, t_{n+1}]$. To complicate the situation even further, part of these boundaries may lie in the vacuum region. Note that the fluxes across these boundaries determine the outflow from the avalanche body, so inappropriate cell reconstructions over the margin cell may cause too much outflow from the avalanche body or even result in a negative depth around the margin; see Fig. 5a. Thus, the difficulty is not only in determining

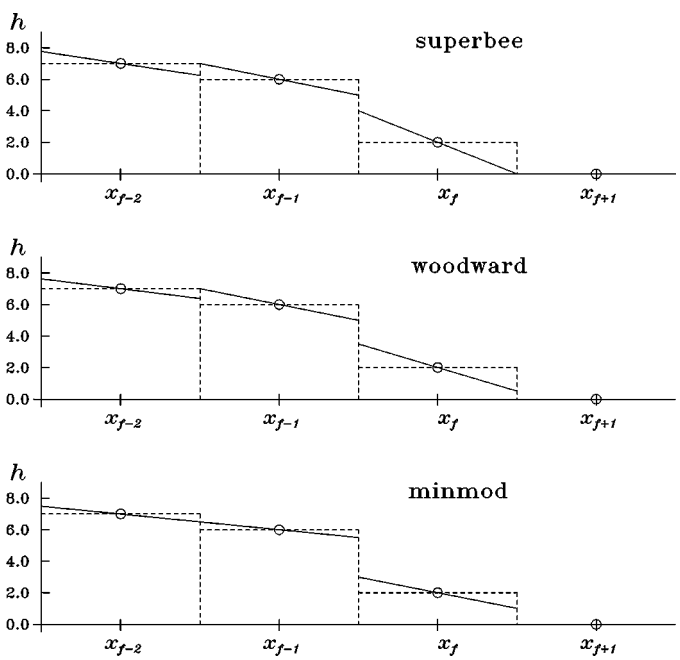

FIG. 4. Example of the depth reconstruction (solid line) determined by different TVD limiters, where the circles denote the cell average. The front margin lies in the fth cell. In the Eulerian scheme one cannot determine where the margin lies. Outside the margin there is no material, so that the average depths of the cells $f + i$, $i \ge 1$ are equal to zero. Different limiters lead to different outflows from the avalanche body.

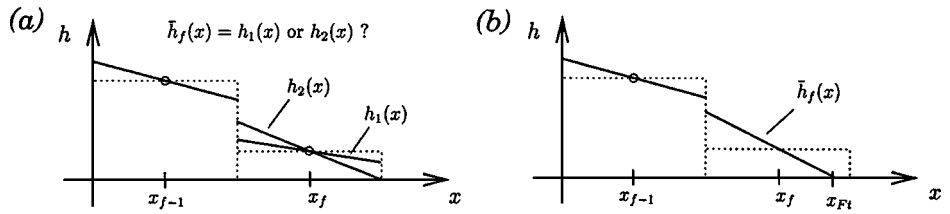

FIG. 5. The reconstruction of the depth $\bar{h}_f(x)$ within the margin fth cell. (a) Cell reconstructions based on TVD limiters cannot determine the location of the margin point. Inappropriate reconstructions over the margin cell may result in wrong values of the flux at the gridpoint x_f, which may cause too much outflow from the avalanche body. (b) Our front-tracking method uses the unique piecewise linear reconstruction $\bar{h}_f(x)$ over the margin cell, which vanishes at the margin point x_{Ft} and preserves the cell average. Thus, a reasonable flux at x_f is expected.

the correct numerical flux at the grid point x_f; the wrong numerical flux may also cause vast stability problems. Adding a thin layer over the whole computational domain can circumvent the numerical stability problem, but it is then difficult to determine the locations of the margins, and the numerical flux out of the avalanche body may even become unexpectedly large, which results in large numerical diffusion, while there will be permanent outflow from the avalanche body. Therefore, a more refined treatment of the evolution of the avalanche margins is needed.

In [29], Munz developed a method for tracking vacuum fronts in gas dynamics. His approach is based on appropriate reconstructions of cell averages behind the front and on the solution of a vacuum Riemann problem, which is used to track the margin locations at every time step. Here we develop an alternative front-tracking method, which is based on a piecewise linear spatial reconstruction of the conservative variables up to the front and Taylor extrapolations in time. Contrary to [29] our approach is Riemann-solver free and therefore fits perfectly into the framework of central schemes.

The structure of our front-tracking algorithm is as follows: At the beginning of each time step (at time t_n), the cell averages $\bar{\mathbf{w}}_j^n$ of the conservative variables and the position of the margin points x_{Ft}^n (front) and x_{Tl}^n (tail) are given. In the first step, a piecewise linear reconstruction of the data is defined, the front (tail) velocity is determined, and the front (tail) is propagated from time t_n to t_{n+1}. In the second step, the conservative variables are updated via

$$\bar{\mathbf{w}}_{j-1/2}^{n+1} = \frac{1}{\Delta x}\int_{x_{j-1}}^{x_j} \mathbf{w}(x, t^n)\, dx - \frac{1}{\Delta x}\int_{t^n}^{t^{n+1}} \{\mathbf{f}(x_j, t) - \mathbf{f}(x_{j-1}, t)\}\, dt + \frac{1}{\Delta x}\int_{t^n}^{t^{n+1}}\int_{x_{j-1}}^{x_j} \mathbf{s}(x, t)\, dx\, dt. \tag{50}$$

Away from the front, the integrals are evaluated by the midpoint rule as in (42). Special care has to be taken in the two margin cells (the cells containing the front and the tail). Each of the integrals on the RHS of (50) may contain parts of the vacuum region. Therefore, we need to replace the midpoint rule by more delicate quadrature rules over the region covered by the granular material.

In order to guide the reader through the details of the algorithm, we give an outline of the rest of this section. In Section 4.1, a particular piecewise linear reconstruction of

the conservative variables near the front is derived. In Section 4.2, the front velocities are computed, and the fronts are propagated to the new time level. In Section 4.3, four cases are distinguished for the location of the front relative to the fixed underlying grid, and their geometry is discussed. In Sections 4.4–4.6, the three integrals on the RHS of (50) are treated: the data, the fluxes, and the source terms. In Section 4.7, a special space–time Taylor extrapolation of the conservative variables near the front, which is needed to compute the solution at the space–time quadrature points of the three integrals, is derived. Section 4.8 summarizes the algorithm.

4.1. Reconstructing the Conservative Variables

In the following we focus on the front margin. The rear margin can be treated completely analogously. Suppose as before that the front margin is contained in the fth cell,

$$x_{Ft}^n \in (x_{f-1/2}, x_{f+1/2}].$$

We require that the piecewise linear reconstruction $\bar{\mathbf{w}}(x, t_n)$ satisfy the following two criteria:

- first, it should vanish at the margin points, and
- second, it should preserve the cell averages.

These criteria uniquely determine the reconstruction in the margin cells. If we denote the cell-averaged depths of the front margin cell by h_f, then the depth reconstruction is defined by

$$\bar{h}_f(x) = \frac{x - x_{Ft}}{\Delta x}\bar{h}'_f; \quad \bar{h}'_f = \frac{-2h_f}{(\Delta x_{Ft}/\Delta x)^2}, \quad \text{for } x \in (x_{f-1/2}, x_{Ft}]. \tag{51}$$

Outside the margin the depth is equal to zero. The x_{Ft} and $x_{f-1/2}$ represent the locations of the front and the internal boundary of the front margin cell, respectively (see Fig. 5), and $\Delta x_{Ft} := x_{Ft} - x_{f-1/2}$ is its length. The reconstruction of $m = hu$, $\bar{m}(x)$, is defined analogously. Note that in (51), the denominator $\Delta x_{Ft}/\Delta x$ may in principle become arbitrarily small which could cause numerical instability. However, we will see in Section 4.7 that in those cases where the numerical derivatives $\bar{h}'_f$ and $\bar{m}'_f$ are actually used, $\Delta x_{Ft}/\Delta x$ will be bounded away from zero.

4.2. Propagating the Front

Our definition of the reconstructions of the conservative variables h and m over the margin cells leads to a constant reconstruction of the velocity over the margin cells,

$$u(x, t_n) = \frac{\bar{m}_f(x)}{h_f(x)} = \frac{\bar{m}'_f(x - x_{Ft})/\Delta x}{\bar{h}'_f(x - x_{Ft})/\Delta x} = \frac{m_f}{h_f},$$

so it would seem natural to define the margin velocity by the constant value

$$u_{Ft}^n = \frac{m_f}{h_f}. \tag{52}$$

However, this assignment would have two disadvantages: first, it is only first-order accurate. Second, as can be seen from (51), the terms m_f and h_f are on the order of

$$\mathcal{O}(\Delta x)\mathcal{O}((\Delta x_{Ft}/\Delta x)^2).$$

Depending on the location of the front relative to the grid, the latter term can become arbitrarily small. Dividing these small numbers in (52) may result in large errors for the front velocity.

Therefore we replace (52) by the simple Taylor extrapolation

$$u_{Ft}^n = u_{f-1} + (\Delta x/2 + \Delta x_{Ft})(u_{f-1} - u_{f-2}), \tag{53}$$

where $u_j := m_j/h_j$. This assignment is both numerically stable and second-order accurate in space. In order to obtain second-order accuracy in time, as well, we approximate the margin velocity at time $t^{n+1/2}$. Using the evolution equation (4) for the velocity we define

$$u_{Ft}^{n+1/2} = u_{Ft}^n + \frac{\Delta t}{2\Delta x}\left(s_f^n \Delta x - \beta_x \bar{h}_f'\right). \tag{54}$$

Here we have used the fact that h vanishes at the front. The location of the margin at the new time level is then given by

$$x_{Ft}^{n+1} = x_{Ft}^n + \Delta t\, u_{Ft}^{n+1/2}. \tag{55}$$

4.3. Intersecting the Front and the Grid

Once the new location of the margin is given, the new margin cell at the next time step is then determined. The CFL condition (49) guarantees that $|u_{Ft/Tl}^n \Delta t| < \Delta x/2$, so the margin point $x_{Ft/Tl}$ can at most pass through gridpoint $x_{f/t}$ during one time step. For example, with this condition the front can only lie in one of the two cells adjacent to the margin fth cell, which are the $(f - \frac{1}{2})$th and $(f + \frac{1}{2})$th cells; see Fig. 6. There are four possible cases for the motion of the front margin point,

- case I: $x_{Ft}^n \le x_f$ and $x_{f-1} < x_{Ft}^{n+1} \le x_f$,
- case II: $x_{Ft}^n > x_f$ and $x_f < x_{Ft}^{n+1} \le x_{f+1}$,
- case III: $x_{Ft}^n \le x_f$ and $x_f < x_{Ft}^{n+1} \le x_{f+1/2}$,
- case IV: $x_{Ft}^n > x_f$ and $x_{f-1/2} < x_{Ft}^{n+1} \le x_f$,

where x_{Ft}^n and x_{Ft}^{n+1} are the front locations at t^n and t^{n+1}, respectively. In cases I and II, the front does not pass gridpoint x_f, while in cases III and IV it does; see Fig. 6. In each case we have to determine the cell averages of the relevant cells $\bar{\mathbf{w}}_{f-1/2}^{n+1}$ and $\bar{\mathbf{w}}_{f+1/2}^{n+1}$ by integrating the governing equations over $[x_{f-1}, x_f] \times [t^n, t^{n+1}]$ and $[x_f, x_{f+1}] \times [t^n, t^{n+1}]$, respectively; i.e., we have to evaluate the three integrals on the RHS of (50). These integrals involve the data $\mathbf{w}$, the fluxes $\mathbf{f}$, and the source term $\mathbf{s}$. In the following, we derive quadrature rules which are exact for linear functions. The tail margin can be treated completely analogously.

4.4. The Integral of the Data

First we integrate the linear reconstruction $\mathbf{w}(x, t_n)$ of the data at time t_n over the interval $[x_{f-1}, x_f]$. In cases I and III, this interval contains the front, while it does not in cases II and IV. We obtain

$$\frac{1}{\Delta x}\int_{x_f}^{x_{f-1}} \mathbf{w}(x, t^n)\, dx = \begin{cases} \frac{1}{2}\bar{\mathbf{w}}_{f-3/4} + \bar{W}_f^n & \text{in cases I and III} \\ \frac{1}{2}\left(\bar{\mathbf{w}}_{f-3/4} + \bar{\mathbf{w}}_{f-1/4}^n\right) & \text{in cases II and IV.} \end{cases} \tag{56}$$

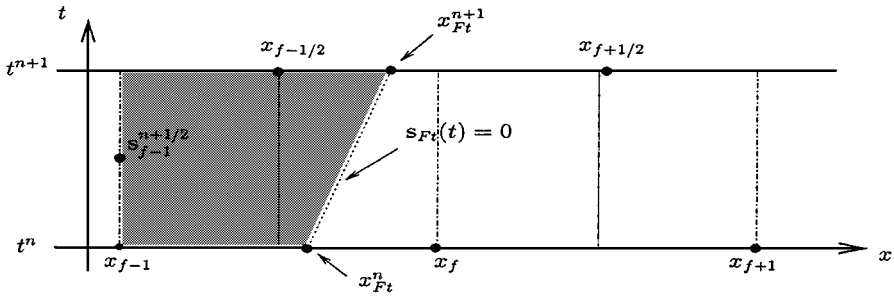

case I

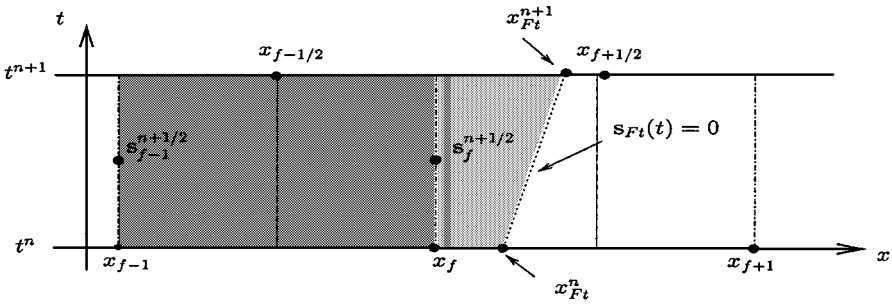

case II

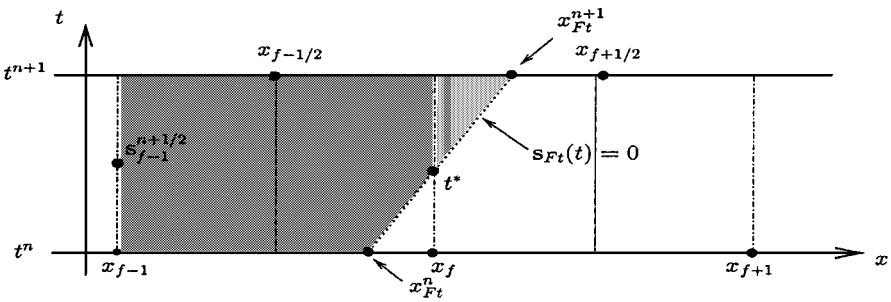

case III

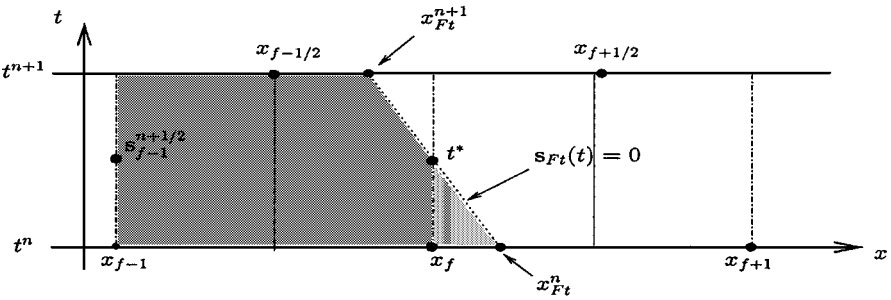

case IV

FIG. 6. The four cases for the propagation of the front margin.

Here $\bar{\mathbf{w}}_{f-3/4}$ is given by (43) and $\mathbf{w}^n_{f-1/4}$ by (51). With a given front location x^n_{Ft} and $\bar{\mathbf{w}}^n_f$ it is

$$\mathbf{w}^n_{f-1/4} = 2\bar{\mathbf{w}}^n_f \left\{ 1 - \left(\frac{x^n_{Ft} - x_f}{x^n_{Ft} - x_{f-1/2}} \right)^2 \right\}. \tag{57}$$

Next we consider the integral over the interval $[x_f, x_{f+1}]$. Using (51) once more we obtain

$$\frac{1}{\Delta x} \int_{x_{f+1}}^{x_f} \mathbf{w}(x, t^n)\, dx = \begin{cases} 0 & \text{in cases I and III} \\ \bar{\mathbf{w}}^n_f \left(\frac{x^n_{Ft} - x_f}{x^n_{Ft} - x_{f-1/2}} \right)^2 & \text{in cases II and IV.} \end{cases} \tag{58}$$

4.5. The Integral of the Fluxes

Due to the restriction of the time step, the only grid position which is possibly intersected by the front during the time interval $[t_n, t_{n+1}]$ is $x = x_f$. Therefore, the flux at x_{f-1} can be evaluated exactly as in the interior of the domain,

$$\frac{1}{\Delta t} \int_{t_{n+1}}^{t_n} \mathbf{f}(\mathbf{w}(x_{f-1},\, t))\, dt = \mathbf{f}^{n+1/2}_{f-1}, \tag{59}$$

where $f^{n+1/2}_{f-1}$ is given by (44). The flux at x_{f+1} vanishes, since this point lies in the vacuum region during the whole time interval. It remains to compute the flux at x_f. In cases III and IV, where the front crosses x_f, we use the midpoint rule in time over that part of the interface which lies within the region covered by granular material. Let $\bar{t}$ and $\overline{\Delta t}$ be the midpoint and the length of this time interval. If t^* is the time at which the front intersects x_f, defined by

$$x^n_{Ft} + (t^* - t_n) u^n_{Ft} = x_f, \tag{60}$$

then

$$\bar{t} = \begin{cases} (t_{n+1} + t^*)/2 & \text{in case III} \\ (t_n + t^*)/2 & \text{in case IV} \end{cases} \tag{61}$$

and

$$\overline{\Delta t} = \begin{cases} t_{n+1} - t^* & \text{in case III} \\ t^* - t_n & \text{in case IV.} \end{cases} \tag{62}$$

The midpoint rule for the flux now gives

$$\frac{1}{\Delta t} \int_{t_{n+1}}^{t_n} \mathbf{f}(\mathbf{w}(x_f, t)\, dt = \begin{cases} 0 & \text{in case I} \\ \mathbf{f}^{n+1/2}_f & \text{in case II} \\ \frac{\overline{\Delta t}}{\Delta t} \mathbf{f}^{\bar{t}}_f & \text{in cases III and IV.} \end{cases} \tag{63}$$

Here $\mathbf{f}^{\bar{t}}_f = \mathbf{f}(\mathbf{w}(x_f, \bar{t}))$. In Section 4.7 we will extrapolate the solution $\mathbf{w}$ to the quadrature point $(x_f, \bar{t})$.

4.6. The Integral of the Source Term

The source term **s** has to be integrated over the quadrilateral regions shown in Fig. 6. Let us call these areas of integration Ω. In the following lemma, we give a quadrature rule which is exact for linear functions vanishing at the front.

LEMMA 4.1. *Let* $a, b, \tau \geq 0$ *and*

$$\Omega := \{(x,t) : \hat{t} \leq t \leq \hat{t} + \tau, \hat{x} \leq x \leq \hat{x} + a + (b-a)(t-\hat{t})/\tau\}.$$

Let **s** *be a linear function over* Ω *which vanishes at the boundary* $x = \hat{x} + a + (b-a)(t-\hat{t})/\tau$. *Then*

$$\iint_{\Omega} \mathbf{s}(x,t)\,dx\,dt = \frac{1}{3}\tau\frac{a^2+ab+b^2}{a+b}\mathbf{s}(\hat{x},\hat{t}+\tau/2) =: \omega\mathbf{s}(\hat{x},\hat{t}+\tau/2). \tag{64}$$

Proof. W.l.o.g. let $\hat{x} = \hat{t} = 0$. The general form of **s** is given by

$$\mathbf{s}(x,t) = (x - a - (b-a)t/\tau)\sigma,$$

where σ is a real constant. W.l.o.g. let $\sigma = 1$. Then a direct computation gives that

$$\iint_{\Omega} \mathbf{s}(x,t)\,dx\,dt = -\frac{\tau}{6}(a^2+ab+b^2) = \omega\mathbf{s}\left(0, \frac{\tau}{2}\right).$$

□

Equation (64) may be interpreted as a special quadrature rule with node $(\hat{x}, \hat{t}+\tau/2)$. We have chosen this node because it appears also in the quadrature rule for the fluxes treated in Section 4.5, so we can minimize the evaluations of the solution **w**.

In the following we apply the lemma to the four cases. Let $\bar{\Omega}$ be the region covered by the granular material. First, we compute the integral over the intersection of $\bar{\Omega}$ with the union of the $(f-1/2)$th and the $(f+1/2)$th cell, $\Omega = \bar{\Omega} \cap ([x_{f-1}, x_{f+1}] \times [t^n, t^{n+1}])$. Using $\hat{x} = x_{f-1}$, $\hat{t} = t_n$, $a = x^n_{Ft} - x_{f-1}$, $b = x^{n+1}_{Ft} - x_{f-1}$, and $\tau = \Delta t$ in Lemma 4.1 gives

$$\int_{t^n}^{t^{n+1}} \int_{x_{f-1}}^{x_{f+1}} \mathbf{s}(x,t)\,dx\,dt = \omega_{f-1}\mathbf{s}^{n+1/2}_{f-1} \tag{65}$$

with

$$\omega_{f-1} = \frac{\Delta t}{3}\frac{\left(x^n_{Ft} - x_{f-1}\right)^2 + \left(x^n_{Ft} - x_{f-1}\right)\left(x^{n+1}_{Ft} - x_{f-1}\right) + \left(x^{n+1}_{Ft} - x_{f-1}\right)^2}{x^n_{Ft} + x^{n+1}_{Ft} - 2x_{f-1}}. \tag{66}$$

Similarly, for the integral over $\bar{\Omega} \cap ([x_f, x_{f+1}] \times [t^n, t^{n+1}])$ we obtain

$$\int_{t^n}^{t^{n+1}} \int_{x_f}^{x_{f+1}} \mathbf{s}(x,t)\,dx\,dt = \omega_f \bar{\mathbf{s}^t_f}, \tag{67}$$

where $\bar{t} = t^{n+1/2}$ in cases I and II and $\bar{t}$ is given by (61) in cases III and IV, and the weight is given by

$$\omega_f = \begin{cases} 0 & \text{in case I} \\ \frac{\Delta t}{3} \frac{\left(x^n_{Ft} - x_f\right)^2 + \left(x^n_{Ft} - x_f\right)\left(x^{n+1}_{Ft} - x_f\right) + \left(x^{n+1}_{Ft} - x_f\right)^2}{x^n_{Ft} + x^{n+1}_{Ft} - 2x_f} & \text{in case II} \\ \frac{\overline{\Delta t}}{3}\left(x^{n+1}_{Ft} - x_f\right) & \text{in case III} \\ \frac{\overline{\Delta t}}{3}\left(x^n_{Ft} - x_f\right) & \text{in case IV.} \end{cases} \tag{68}$$

Here $\overline{\Delta t}$ is given by (62). The integral over $[x_{f-1}, x_f] \times [t^n, t^{n+1}]$ is then computed by substracting the integral over $[x_f, x_{f+1}] \times [t^n, t^{n+1}]$ from that over $[x_{f-1}, x_{f+1}] \times [t^n, t^{n+1}]$,

$$\int_{t^n}^{t^{n+1}} \int_{x_{f-1}}^{x_f} \mathbf{s}(x,t)\, dx\, dt = \omega_{f-1}\mathbf{s}^{n+1/2}_{f-1} - \omega_f \mathbf{s}^{\bar{t}}_f. \tag{69}$$

This completes the definition of the quadrature rules for the three integrals on the RHS of (50). It remains to extrapolate the solution $\mathbf{w}$ to the new quadrature point $(x_f, \bar{t})$ near the front.

4.7. Determination of the Physical Quantities at $\bar{t}$

In cases III and IV the margin point passes the cell boundary x_f at t^* and goes into the neighboring cell. The outflow in case III and the inflow in case IV through the cell boundary at x_f as well as the source term in the new and old margin cells are essential for determining the cell average of the margin cells in the front-tracking method.

In case III the physical quantities flow through the boundary x_f into the $(f + \frac{1}{2})$th cell during the time interval $[t^*, t^{n+1}]$. The outflow is approximated by the value at $(x_f, \bar{t})$, where $\bar{t} = \frac{1}{2}(t^{n+1} + t^*)$. Note that

$$x_{Ft}(\bar{t}) = x^n_{Ft} + u^{n+1/2}_{Ft}(\bar{t} - t^n), \quad h(x_{Ft}(\bar{t}), \bar{t}) = 0$$
$$\frac{\partial}{\partial x} h(x_{Ft}(\bar{t}), \bar{t}) = \frac{1}{\Delta x}\bar{h}'_f + \mathcal{O}(\Delta t).$$

Therefore,

$$h^{\bar{t}}_f = h(x_f, \bar{t}) = \frac{\left(x_f - x^n_{Ft}\right) - u^{n+1/2}_{Ft}(\bar{t} - t^n)}{\Delta x}\bar{h}'_f \tag{70}$$

and similarly

$$m^{\bar{t}}_f = m(x_f, \bar{t}) = \frac{\left(x_f - x^n_{Ft}\right) - u^{n+1/2}_{Ft}(\bar{t} - t^n)}{\Delta x}\bar{m}'_f. \tag{71}$$

In case IV the physical quantities at the boundary $(x_f, \bar{t})$ are determined in the same way, but the time points are defined differently: $\bar{t} = (t^{n+1} + t^*)/2$ for case III and $\bar{t} = (t^n + t^*)/2$ for case IV. In (70) the numerical derivative $\bar{h}'_f$ is given by (51). We now check that the

denominator $(\Delta x_{Ft}/\Delta x)^2$ in (51) is bounded away from zero: In case III, $\Delta x_{Ft}/\Delta x > 1/2$ (see Fig. 6), and in case IV,

$$\frac{\Delta x_{Ft}}{\Delta x} > \frac{1}{2} - \frac{\Delta t}{\Delta x} u_{Ft}^{n+1/2} > \frac{1}{2} - \mathrm{CFL},$$

where CFL is the Courant number, i.e., the left-hand side of Eq. (49).

4.8. Summary of the Front-Tracking Algorithm

The front-tracking algorithm may be summarized as follows:

$$\bar{\mathbf{w}}_{f-1/2}^{n+1} = \frac{1}{2}\bar{\mathbf{w}}_{f-3/2}^{n} + (1-\alpha_f)\bar{\mathbf{w}}_f^n - \frac{\overline{\Delta t}}{\Delta x}\bar{\mathbf{f}}_f^{\bar{t}} + \frac{\Delta t}{\Delta x}\mathbf{f}_{f-1}^{n+1/2} \tag{72}$$

$$+ \frac{\omega_{f-1}}{\Delta x}\mathbf{s}_{f-1}^{n+1/2} - \frac{\omega_f}{\Delta x}\bar{\mathbf{s}}_f^{\bar{t}} \tag{73}$$

$$\bar{\mathbf{w}}_{f+1/2}^{n+1} = \alpha_f \bar{\mathbf{w}}_f^n + \frac{\overline{\Delta t}}{\Delta x}\bar{\mathbf{f}}_f^{\bar{t}} + \frac{\omega_f}{\Delta x}\bar{\mathbf{s}}_f^{\bar{t}}. \tag{74}$$

Here

$$\alpha_f = \begin{cases} 0 & \text{in cases I and III} \\ \left(\frac{x_{Ft}^n - x_f}{x_{Ft}^n - x_{f-1/2}}\right)^2 & \text{in cases II and IV} \end{cases} \tag{75}$$

$$\overline{\Delta t} = \begin{cases} 0 & \text{in case I} \\ \Delta t & \text{in case II} \\ t_{n+1} - t^* & \text{in case III} \\ t^* - t_n & \text{in case IV} \end{cases} \tag{76}$$

$$\bar{t} = \begin{cases} t_n & \text{in case I} \\ t_{n+1/2} & \text{in case II} \\ (t_{n+1} + t^*)/2 & \text{in case III} \\ (t_n + t^*)/2 & \text{in case IV.} \end{cases} \tag{77}$$

The weights ω_{f-1} and ω_f are defined in (66) and (68). The values of $\mathbf{w}(x_f, \bar{t})$, needed to determine $\bar{\mathbf{f}}_f^{\bar{t}}$ and $\bar{\mathbf{s}}_f^{\bar{t}}$, are defined in (70) and (71). This completes the definition of the update at the front margin. The tail can be treated completely analogously.

5. NUMERICAL RESULTS

In the following we present some numerical experiments. In Section 5.1 we compute a travelling shock wave. In this case the Lagrangian method leads to oscillatory solutions travelling at the wrong speed, while the NOC scheme yields correct sharp monotone shock profiles. In Section 5.2 we compute the parabolic similarity solution. Here the Lagrangian technique is superior to the NOC scheme unless the latter is equipped with the front-tracking technique. We also discuss a tendency of the NOC scheme with piecewise linear spatial reconstructions to produce small oscillations near smooth local maxima and show how to remove these oscillations by using piecewise quadratic reconstructions. In the final

numerical experiment in Section 5.3 we compute an avalanche with a vacuum front at the margins, which forms an upward-propagating shock wave when it comes to a halt at a flat runout. Our NOC front-tracking scheme gives a stable and accurate approximation of this challenging flow.

5.1. Travelling Shock Wave

In this test problem we are concerned with granular flow on a plane ($\lambda\kappa = 0$) inclined chute ($0 \le x \le 36$ dimensionless units), where the internal and basal friction angles are both presumed to be equal to the inclination angle, $\phi = \delta = \zeta = 40^\circ$. That implies a nonaccelerative flow, $s_x = 0$, whose earth pressure coefficient is constant $K_x = K_{x_{act}} = K_{x_{pass}}$. Selecting $\varepsilon = 1$ and using (6) yields $\beta_x = \varepsilon \cos\zeta K_x = 1.84477$. A jump of thickness $H = h^-/h^+ = 3$ with $h^+ = 0.3$, $h^- = 0.9$ is presumed at $x = 24$. By virtue of (12) the velocity difference is then determined, $u^+ - u^- = 1.2148317$, where the positive sign is selected. Since an instability was expected close to $u = 0$ as a singularity by $\mathrm{sgn}(u)$, the downslope velocity is assumed to be $u^- = 0.1$, so that the term $\mathrm{sgn}(u)$ is always unity. The initial condition of this test problem is defined as

$$h(x,0) = \begin{cases} 0.3, & \text{for } 0 \le x < 24, \\ 0.9, & \text{for } 24 \le x < 36, \end{cases} \tag{78}$$

$$u(x,0) = \begin{cases} 1.3148317, & \text{for } 0 \le x < 24, \\ 0.1, & \text{for } 24 \le x \le 36. \end{cases} \tag{79}$$

From (13) the velocity of the upslope travelling wave is then expected as $V_n = -0.50741585$. For the boundary condition a constant inflow at $x = 0$ and an outflow condition at $x = 36$ are introduced.

5.1.1 *Lagrangian Technique*

By the Lagrangian moving grid method the governing equations (1) and (4) are solved by virtue of (34)–(37). The initial depth, h_j^0, of the jth element is taken to be the cell average of the exact initial profile. The initial velocity of the boundary, u_j^0, is given by the volume weighted velocity of the adjacent cells. They are

$$h_j^0 = \frac{\int_{b_{j-1}^0}^{b_j^0} h(x,0)\,dx}{b_j^0 - b_{j-1}^0}, \quad u_j^0 = \frac{\int_{c_j^0}^{c_{j+1}^0} h(x,0)u(x,0)\,dx}{\int_{c_j^0}^{c_{j+1}^0} h(x,0)\,dx}, \tag{80}$$

where b_j^0 and b_{j-1}^0 are the boundaries of the jth cell at $t = 0$, and c_j^0 denotes the initial centre of the jth cell.

The constant inflow and outflow boundary conditions are executed by setting the depth gradient $\partial h/\partial x$ at $x = b_0(t)$ and $x = b_N(t)$ equal to zero, so that $du/dt = 0 \Rightarrow u_0(t) = u_0(0)$ and $u_N(t) = u_N(0)$ for $t > 0$ because the flow is on a nonaccelerating slope $s_x = 0$.

Figure 7 demonstrates the simulated results ($N = 60$); oscillations develop as the shock wave passes through, and these persist even if the time step is selected to be very small. The velocities of the cell boundary after the shock are sometimes faster or slower than

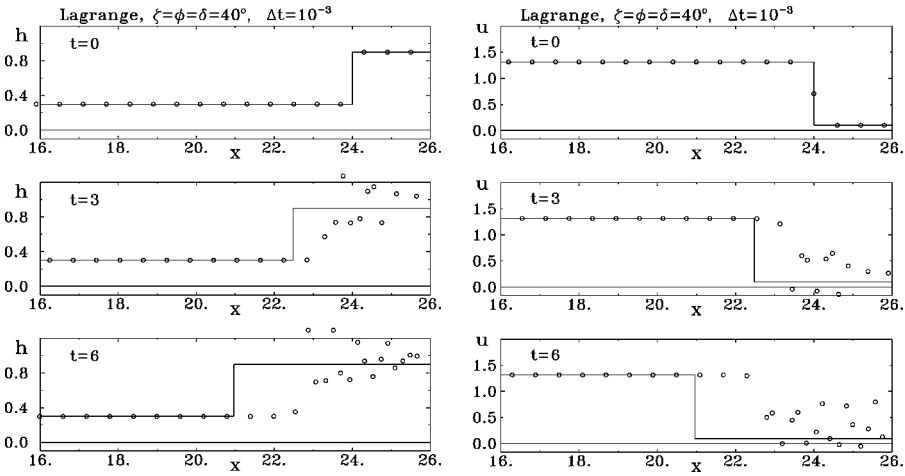

FIG. 7. Depth (left) and the corresponding velocity (right) profiles of the upslope travelling wave at $t = 0, 3, 6$, where circles denote the computed results at the cell centres and the solid line indicates the exact solution. The time step is taken to be $\Delta t = 10^{-3}$ dimensionless time unit.

they should be and therefore oscillations take place. These oscillations propagate downslope as time increases and no shock wave propagates upslope. This indicates that the Lagrangian moving grid technique is ill behaved and cannot describe the travelling shock wave.

5.1.2 *Eulerian Shock-Capturing Methods*

The NOC scheme is applied to (1) and (2) on a 1D grid with 90 and 360 gridpoints, respectively. The initial conditions are transferred to the mean values over the cells before the computing commences,

$$h_j^0 = \frac{1}{\Delta x}\int_{x_{j-1/2}}^{x_{j+1/2}} h(x,0)\,dx, \quad u_j^0 = \frac{1}{h_j^0}\int_{x_{j-1/2}}^{x_{j+1/2}} h(x,0)u(x,0)\,dx. \tag{81}$$

The constant-inflow boundary condition is implemented by the assignments $h_0(t) = h_0(0)$ and $m_0(t) = m_0(0)$ at $x = 0$. The outflow boundary condition is described by setting $\partial h/\partial x = 0$ and $\partial m/\partial x = 0$ at $x = 36$, where they are

$$U_N = (4U_{N-1} - U_{N-2})/3, \quad \text{for } U = h, m, \tag{82}$$

by using the cell averages of the closest cells for a second-order extrapolation.

Three different cell reconstructions were tested: the NOC scheme with Superbee limiter (NOCS-S), piecewise linear ($r = 2$), and quadratic ($r = 3$) WENO reconstructions [26]. Figure 8 demonstrates the simulated avalanche depth of the travelling wave problem (circles) and a comparison with the exact solution (solid line) at $t = 6$ dimensionless time units. All of them are able to adequately describe this travelling shock wave problem.

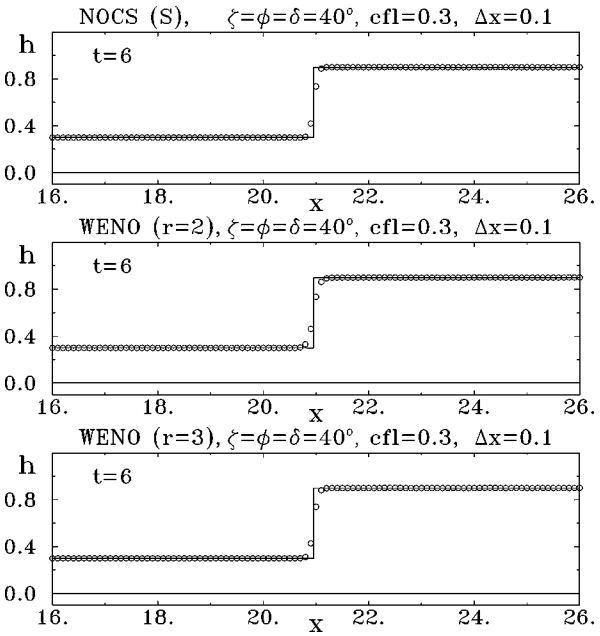

FIG. 8. Depth profiles of the upslope travelling wave computed by the NOC scheme at $t = 6$ with $N = 360$. The solid lines indicate the exact solution and circles mean the computed results.

5.2. Parabolic Similarity Solution

This section is concerned with the simulation of the parabolic similarity solution outlined in Section 2.2. In the test problem the parabolic avalanche body is considered to slide on an inclined flat plane in the domain $0 \le x \le 36$ dimensionless length units with constant inclination angle $\zeta = 40^\circ$. The basal and internal friction angles are simultaneously selected to be 30°, and the initial condition is chosen to be $g_0 = 1$ and $p_0 = 0$. On the inclined plane the initial depth and velocity distributions are mapped into

$$\left.\begin{aligned} h(x,0) &= 1 - ((x-4)/3.2)^2 \\ u(x,0) &= 1.2 \end{aligned}\right\} \quad \text{for } x \in [0.8, 7.2]. \tag{83}$$

Our choice of the initial velocity, $u(x,0) = u_0 = 1.2$, guarantees that condition (32) will be satisfied for all times. This problem will serve as the standard test problem for the resolution of the depth profile and the determination of the margin locations.

5.2.1 *Lagrangian Technique*

In the Lagrangian moving grid technique the model equations (1) and (4) are solved by virtue of (34)–(37) on a 1D grid. The boundary condition is given by setting the heights at the margin (front and rear) points to be equal to zero, $h_0(x,t) = 0$ and $h_N(x,t) = 0$.

Figure 9 illustrates the simulated result at the dimensionless time units $t = 0, 2, 4, 6$ with cell number $N = 16$, in which the circles denote the computed results and the solid line indicates the exact solution. The avalanche body extends as it flows down and still keeps

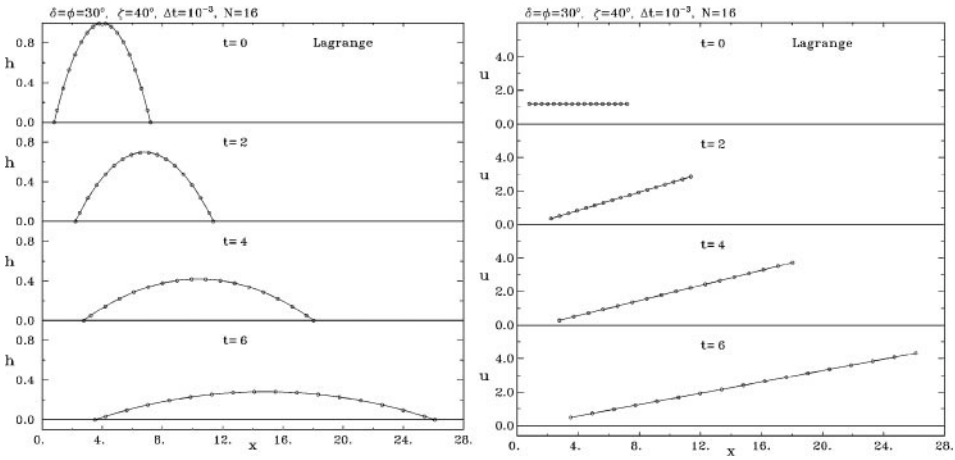

FIG. 9. Depth (left) and the corresponding velocity (right) profiles of the parabolic similarity solution (Problem I) computed by the Lagrangian, moving grid scheme at the dimensionless time units $t = 0$, 2, 4, 6, where the avalanche body is divided into 16 cells, and the time interval is $\Delta t = 10^{-3}$.

the parabolic depth profile. The velocity is keeping a linear distribution through the bulk body. It ensures the symmetric depth profile during the motion.

From the simulated results it follows that the Lagrangian moving grid technique not only describes the depth profile well but also determines the margin locations of the similarity solution very accurately. There is excellent agreement between the simulated results and the exact solutions, see Fig. 9. The motions of the front and rear edges of the avalanche body in the similarity solution are illustrated in Fig.10. The circles denote the computed results by the Lagrangian moving grid technique and the solid lines indicate the exact locations of the margins. They are also in excellent agreement.

The Lagrangian method is also tested by different grid numbers. Figure 11 shows the results computed with different grid numbers, $N = 16$, 32, and 64, respectively. With different

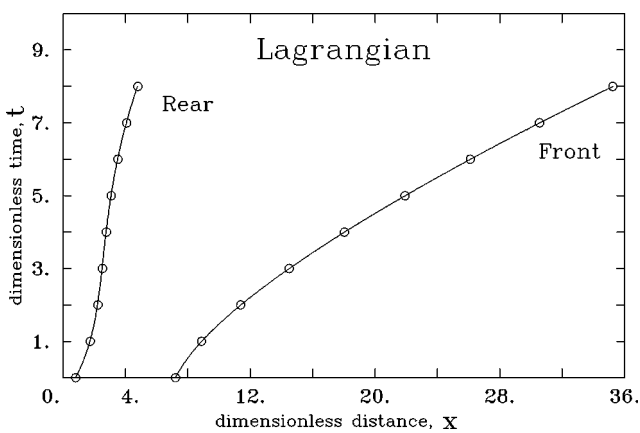

FIG. 10. Locations of the front and rear edges of the avalanche body in the parabolic similarity solution problem as they evolve in time. The circles denote the results computed by the Lagrangian moving-grid technique ($N = 16$), and the solid lines indicate the exact margin positions. They are in excellent agreement.

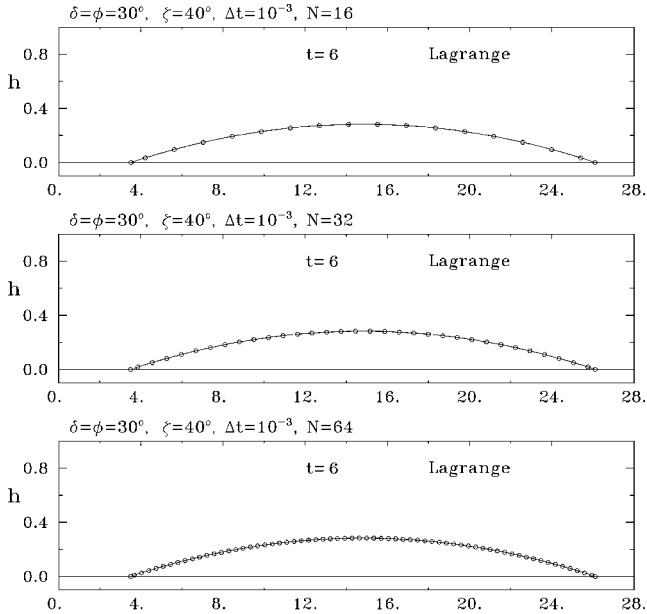

FIG. 11. Depth profiles computed by the Lagrangian moving-grid technique for the parabolic similarity solution problem (Problem l), where the avalanche body is divided into different numbers of cells, $N = 16, 32, 64$. All the results are shown at $t = 6$ and the computational time interval is $\Delta t = 10^{-3}$. The number of the cells does not influence the good agreement between the simulated results (circles) and the exact solutions (solid line).

grid numbers this method can always achieve excellent resolutions when compared with the exact solutions.

Calculations were also performed with initial condition $p_0 \neq 0$; results turned out to be as convincing as the ones above. For this reason they are not presented here [36].

5.2.2 *Eulerian Technique*

In Section 3.2, the Eulerian schemes are based on the model equations (1) and (2) in conservative form, so that the velocity outside the avalanche body (inclusive of the margin point) is not defined. Intuitively, adding a thin layer of material over the whole computational domain could be used to treat grain-free regions. Another trick can also be introduced, in which all the physical variables are set to zero if $h = 0$. This would be reasonable since $h = 0 \rightarrow m = hu = 0$.

Figure 12 illustrates the comparison between the computed results obtained from the NOC scheme, where a thin layer $h_0 = 10^{-4}$, respectively $h_0 = 0$, is added over the whole computational domain, and from the scheme with our front-tracking method. All the three results of the depth profiles are acceptable except for the oscillation near the top. However, a look at the velocity profiles in these figures; there are several cells with $\partial u/\partial x < 0$ around the margins. This violates the assumption $\partial u/\partial x > 0$ in the parabolic similarity solution problem. Moreover, the results show that there is large numerical diffusion around the margins (i.e., the margins move further than they should) without the front-tracking method. For both reasons, the front-tracking method is needed to determine the location of the margins.

Let us discuss the origin of the oscillation near the center of the avalanche. When one recomputes the solution using unlimited central differences for $\bar{\mathbf{w}}'$, the oscillation

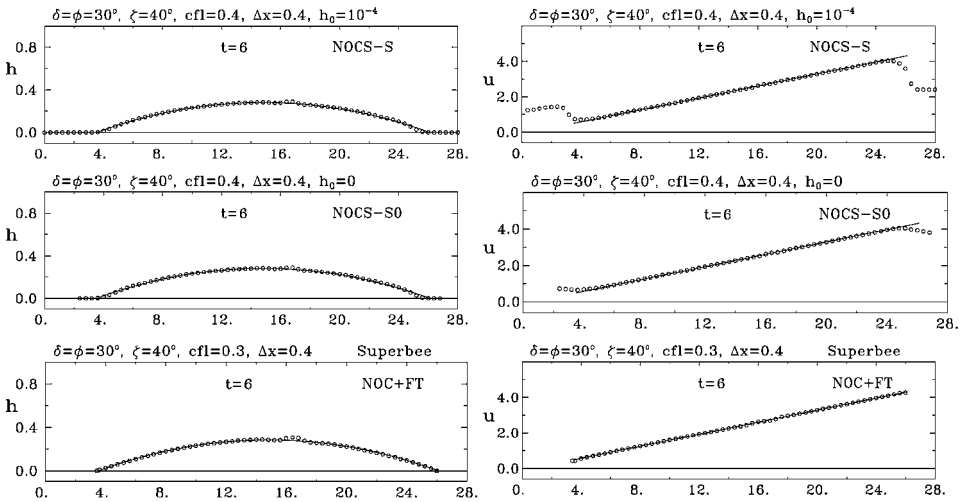

FIG. 12. Depth (left) and velocity (right) profiles of the parabolic similarity solution computed by the NOC scheme with Superbee limiter. In the top panels, a thin layer with $h_0 = 10^{-4}$ is added to the whole computational domain. In the middle panels, all physical variables are set to zero if $h = 0$, while the bottom panels demonstrate the results from the scheme with front-tracking method. The whole computational domain is divided into 90 cells ($N = 90$), the circles denote simulated results and the solid lines represent the exact solution. The results show that the added thin layer does not influence the depth profile very much, if it is sufficiently small, but the margin locations cannot be exactly determined without the front-tracking method. An oscillation near the middle of the avalanche (local maximum) is visible in all three calculations.

disappears. Therefore, we have the following paradoxical situation: the introduction of TVD limiters, which are needed to stabilize the solution in the presence of discontinuities, may destabilize the solution in smooth regions! In fact, this is not entirely surprising, since in the presence of limiters the fluxes depend only Lipschitz-continuously on the data.

We have therefore experimented with smoother reconstructions, namely the piecewise quadratic WENO interpolants of Jiang and Shu [17] and Levy *et al.* [26], which depend smoothly on the data and are at the same time nonoscillatory at discontinuities. In the margin cells, we still use the piecewise linear reconstructions introduced in Section 4.1, and in the two cells adjacent to the margin cells, we use a piecewise linear WENO reconstruction. We have experimented with both second- and third-order quadrature rules in time. In our experience, both yield comparable results. Figure 13 demonstrates the results for these reconstructions combined with our front-tracking method. The margin locations are well described by the front-tracking method, and the oscillation near the center is successfully removed (compare the bottom panels in Figs. 12 and 13).

Figure 14 shows the computed front and rear edges of the avalanche body in the parabolic similarity solution as they evolve in time. "○" denotes the computed results obtained by the NOC scheme with the piecewise quadratic WENO cell reconstruction, "×" means the results deduced with the Superbee limiter and solid lines indicate the exact margin solution. Both the Superbee limiter and the piecewise quadratic WENO cell reconstruction for the NOC front-tracking schemes can yield good agreement of the determined margin locations with the exact solutions.

The use of the Superbee limiter results in a small delay of the avalanche body, i.e., a slower velocity at both the front and the rear. The reason is that the Superbee limiter tends

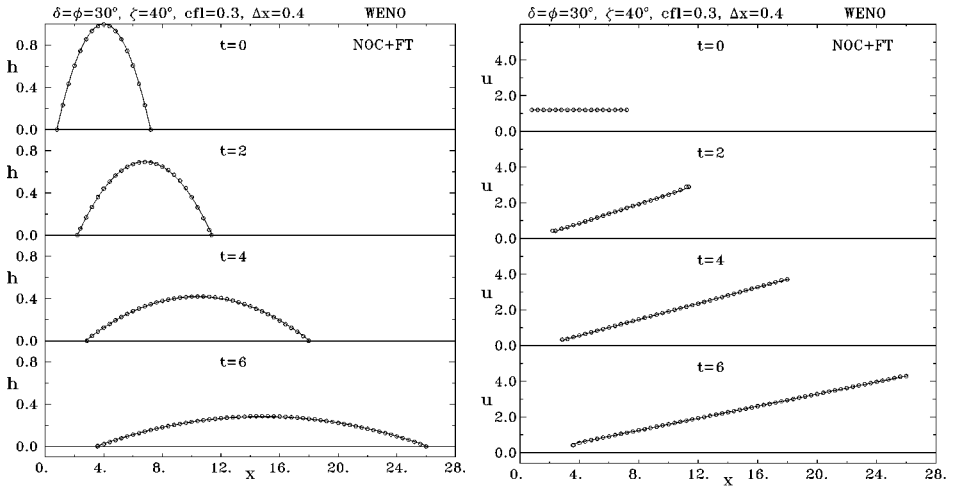

FIG. 13. Depth (left) and velocity (right) profiles of the parabolic similarity solution at $t = 6$ computed by the NOC scheme with front-tracking and piecewise quadratic, WENO cell reconstruction. The whole computational domain is divided into 90 cells ($N = 90$) and the Courant number is selected to be 0.3. The margin locations are well described and the oscillation near the center is successfully removed.

to be overcompressive in smooth regions of the solution, and therefore it does not give the appropriate flux at the boundaries between the internal and the margin cells.

In order to obtain some quantitative information on the accuracy of the schemes, we introduce an error measure for the depth,

$$E = \frac{\sum_{j=0}^{N} \left| h_j - \bar{h}_j^{exact} \right|}{\sum_{j=0}^{N} \bar{h}_j^{exact}}, \tag{84}$$

where $\bar{h}_j^{exact}$ denotes the jth cell-averaged depth of the exact solution. The errors of the

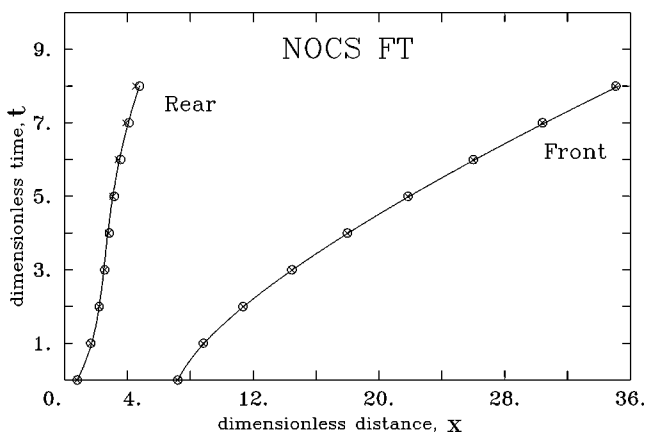

FIG. 14. Front and rear edges of the avalanche body in the parabolic similarity solution simulated by the NOC front-tracking scheme as they evolve in time. "○" denotes the computed results obtained with the piecewise quadratic WENO cell reconstruction; "×" means the results deduced with Superbee limiter, and solid lines indicate the exact margin solution.

TABLE I
Error (84) and Order of Convergence of the Different Schemes

	NFT(90)	NFT(180)	NFT(360)	Order	Lag(16)	Lag(32)	Order
	E ($\times 10^{-4}$)				E ($\times 10^{-4}$)		
$t=1$	6.429	1.023	0.150	2.77	17.130	2.937	2.54
$t=2$	16.521	2.217	0.303	2.87	17.764	3.664	2.28
$t=3$	21.148	2.727	0.338	3.01	18.944	4.135	2.20
$t=4$	23.625	2.776	0.331	3.07	18.888	4.413	2.10
$t=5$	23.449	2.744	0.327	3.07	18.974	4.492	2.08
$t=6$	23.641	2.680	0.318	3.07	19.474	4.658	2.06
$t=7$	23.247	2.641	0.314	3.07	18.817	5.026	1.90
$t=8$	22.648	2.620	0.311	3.07	19.526	4.830	2.02

NOC front-tracking scheme and the Lagrangian method at $t = 1$ to $t = 8$ dimensionless time units are shown in Table I together with their numerical orders of convergence. Here, the Eulerian scheme is tested by using $N = 90$, $N = 180$, and $N = 360$ over the interval [0, 32] and for the Lagrangian scheme $N = 16$ and $N = 32$ are used over the interior of the avalanche, which is a subset of [0, 32]. Since at time $t = 0$ the avalanche has length 7.2, the Eulerian grid of 90 points has precisely 18 points in the interior of the avalanche initially. Therefore, the two coarsest grids are roughly comparable for the two schemes, and so is the error. The Lagrangian scheme is about second-order accurate, as expected. Surprisingly, however, the NOC front-tracking scheme (which is used here with unlimited central differences in the interior of the avalanche) converges with third-order accuracy. Thus, on the grid with 180 points, it is already more accurate than the Lagrangian scheme using 32 points. We have confirmed this convergence rate for grids of 640, 1280, and 2560 points and omit the numbers. This result seems to be one of the rare occurrences of superconvergence, and we do not expect it to be true for general smooth initial data. In any case, it shows that our treatment of the front margin is locally at least second-order accurate—otherwise, the global third-order accuracy of the scheme in the L_1-norm would be destroyed.

5.3. Upward Moving Shock Wave

Shock formations are often observed when the avalanche slides into the run-out horizontal zone. Here the front part comes to rest, while the tail accelerates further and its velocity becomes supercritical. In [38] a comparison was made between our shock-capturing method and the Lagrangian moving grid technique for the case of coinciding basal and internal friction angles. Here we compute a flow with basal friction angle $\phi = 38^\circ$ and internal friction angle $\delta = 35^\circ$. As a consequence, we have a jump in the earth pressure coefficient K_x when the flow changes from an expanding ($u_x > 0$) to a contracting region ($u_x < 0$).

The setup is as follows: The granular material released from a parabolic cap slides down an inclined plane and merges into the run-out horizontal zone. The centre of the cap is initially located at $x = 4.0$ and the initial radius and the height are 3.2 and 1.0 dimensionless length units, respectively. The inclination angle of the inclined plane is 40° and the (linear and continuous) transition region lies between $x = 21.5$ and $x = 25.5$. We use 180 gridpoints and a CFL number of 0.4.

Figure 15 illustrates the simulated process as the avalanche slides on the inclined plane into the horizontal run-out zone (so initially the flow is expanding). The avalanche body

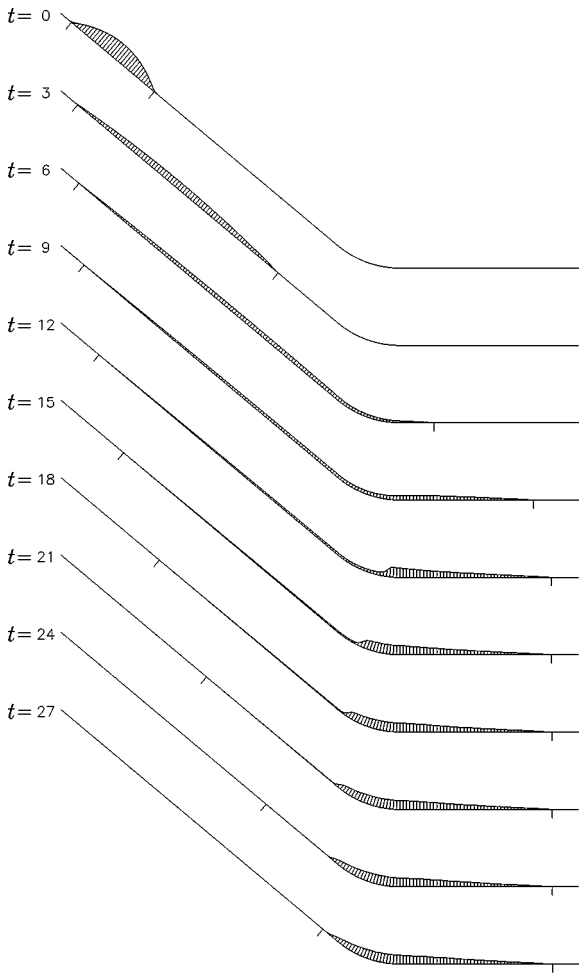

FIG. 15. Process of the avalanche simulated by the shock-capturing and front-tracking NOC method at $t = 0, 3, 6, \ldots, 27$ dimensionless time units. As the front reaches the run-out zone and comes to rest, part of the tail accelerates further and the avalanche body contracts. Once the velocity becomes supercritical,a shock wave develops, which moves upward. The dashes below the graphs mark the tail and the head of the avalanche.

extends on the inclined plane until the front reaches the run-out zone. Here the basal friction is enough to bring the front of the granular material to rest while the rear part accelerates further. Therefore, the flow becomes contracting in the transition zone. At this stage, a shock (surge) wave is created ($t = 12$), which moves upward. Such shock waves make the Lagrangian method unstable, if no artificial viscosity is applied (see [38]). Our nonoscillatory central front-tracking scheme handles both the shock wave and the margins of the avalanche well.

6. CONCLUSION

In this paper we have developed a Lagrangian and an Eulerian shock-capturing finite-difference scheme with front-tracking for the spatially one-dimensional Savage–Hutter equations of granular avalanches. The purpose was to reproduce the temporal evolution of the avalanche geometry and downslope velocity under situations when internal shocks

may occur. This happens, e.g., when an avalanche of finite mass moves from an inclined chute into the horizontal run-out zone and, in the transition zone, is deccelerated from a supercritical flow state to a subcritical state. The Lagrangian scheme (which is excellent for smooth solutions) develops unphysical oscillations when the solution contains, or develops, shock discontinuities. In order to compute discontinuous solutions, we propose to use a conservative shock-capturing finite difference scheme. We adapt the second-order accurate staggered scheme of Nessyahu and Tadmor [30] to the Savage–Hutter equations. The staggered approach avoids the use of characteristic decompositions, which are needed in standard upwind schemes but are not known for the Savage–Hutter equations. We show that our nonoscillatory central scheme reproduces both smooth and shock solutions adequately except for the following two problems: First, oscillations may occur near smooth extrema due to the presence of piecewise linear reconstructions with TVD-type limiters. These oscillations disappear when one uses piecewise quadratic cell reconstructions in the interior of the avalanche. Second, our NOC scheme (and in fact, any Eulerian scheme) does not capture the vacuum boundary accurately. This may lead to serious stability problems. We improve the treatment of the free boundary by combining the scheme with a front-tracking method applied to the margin cells. In the spirit of the Nessyahu–Tadmor scheme, we do not make use of the vacuum Riemann problem but rely on a new piecewise linear reconstruction at the vacuum boundary and carefully chosen Taylor extrapolations for the corresponding numerical fluxes. With such a combination of an internal Eulerian NOC scheme and a Lagrangian "boundary scheme" two standard test problems—an upward moving shock and a parabolic cap moving down an inclined plane—could be well reproduced (indeed, we even observed third-order accuracy for the latter problem). The scheme also produces satisfactory results for the more realistic problem mentioned above: an avalanche moving down an inclined plane and coming to rest at a flat runout. Here an upward moving shock wave develops from smooth data, and the flow changes from expanding to contracting ahead of the shock. In this situation, the earth pressure coefficient changes discontinuously, so we are facing the full difficulties inherent in the Savage–Hutter model.

Several questions remain and await further study:

- The shock-capturing NOC numerical method including the front-tracking scheme should be extended to two-dimensional flows. This is work in progress.
- The original Lagrangian moving grid scheme could also be developed as a shock-capturing scheme. Here the main difficulty would be in the determination of the correct grid velocity.

We are working on these topics and will report on results in due time.

ACKNOWLEDGMENTS

Y. C. Tai, J. M. N. T. Gray, and K. Hutter acknowledge financial support from the Deutsche Forschungsgemeinschaft via SFB 298, "Deformation und Versagen metallischer und granularer Strukturen," at Darmstadt University of Technology. S. Noelle was supported by SFB 256, "Nichtlineare Partielle Differentialgleichungen," at Bonn University.

REFERENCES

1. P. Arminjon and M. C. Viallon, Généralisation du schéma de Nessyahu–Tadmor pour une équation hyperbolique à deux dimensions d'espace, *C. R. Acad. Sci. Paris* **320**, 85 (1995).

2. P. Arminjon and M. C. Viallon, Convergence of a finite volume extension of the Nessyahu–Tadmor scheme on unstructured grids for a two-dimensional linear hyperbolic equation, *SIAM J. Numer. Anal.* **36**, 738 (1999).
3. S. Godunov, A finite difference scheme for numerical computation of discontinuous solutions of equations of fluid dynamics, *Mat. Sb.* **47**, 271 (1959).
4. E. Godlewski and P.-A. Raviart, *Numerical Approximation of Hyperbolic Systems of Conservation Laws* (Springer-Verlag, New York/Berlin/Heidelberg, 1996).
5. J. M. N. T. Gray and K. Hutter, Pattern formation in granular avalanches, *Continuum Mech. Thermodyn.* **9**, 341 (1997).
6. J. M. N. T. Gray and Y. C. Tai, On the inclusion of a velocity dependent basal drag in avalanche models, *Ann. Glaciol.* **26**, 37 (1998).
7. J. M. N. T. Gray and Y. C. Tai, Particle size segregation, granular shocks and stratification patterns, in *Physics of Dry Granular Media*, edited by H. J. Herrmann, J. P. Hovi, and S. Luding, NATO ASI Series (Kluwer Academic, Dordrecht/Norwell, MA, 1998), p. 697.
8. J. M. N. T. Gray, M. Wieland, and K. Hutter, Gravity driven free surface flow of granular avalanches over complex basal topography, *Proc. R. Soc. London Ser. A* **455**, 1841 (1999).
9. R. Greve and K. Hutter, Motion of a granular avalanche in a convex and concave curved chute: Experiments and theoretical predictions, *Proc. R. Soc. London Ser. A* **445**, 399 (1993).
10. R. Greve, T. Koch, and K. Hutter, Unconfined flow of granular avalanches along a partly curved chute. I. Theory, *Proc. R. Soc. London Ser. A* **445**, 399 (1994).
11. A. Harten, High resolution schemes for hyperbolic conservation laws, *J. Comput. Phys.* **49**, 357 (1983).
12. K. Hutter and R. Greve, Two-dimensional similarity solutions for finite-mass granular avalanches with Couloumb- and viscous-type frictional resistence, *J. Glaciol.* **39**, 357 (1993).
13. K. Hutter and T. Koch, Motion of a granular avalanche in an exponentially curved chute: Experiments and theoretical predictions, *Philos. Trans. R. Soc. London Ser. A* **334**, 93 (1991).
14. K. Hutter, T. Koch, C. Plüss, and S. B. Savage, The dynamics of avalanches of granular materials from initiation to runout, *Acta Mech.* **109**, 127 (1995).
15. K. Hutter and Y. Nohguchi, Similarity solutions for a Voellmy model of snow avalanches with finite mass, *Acta Mech.* **82**, 99 (1990).
16. K. Hutter, M. Siegel, S. B. Savage, and Y. Nohguchi, Two-dimensional spreading of a granular avalanche down an inclined plane. I. Theory, *Acta Mech.* **100**, 37 (1993).
17. G. S. Jiang and C. W. Shu, Efficient implementation of weighted ENO schemes, *J. Comput. Phys.* **68**, 151 (1987).
18. G. S. Jiang and E. Tadmor, Nonoscillatory central schemes for multidimensional hyperbolic conservation laws, *SIAM J. Sci. Comput.* **19**, 1892 (1998). [Electronic]
19. T. Koch, R. Greve, and K. Hutter, Unconfined flow of granular avalanches along a partly curved chute. lI. Experiments and numerical computations, *Proc. R. Soc. London Ser. A* **445**, 415 (1994).
20. D. Kröner, *Numerical Schemes for Conservation Laws* (Wiley–Teubner, Chichester/Stuttgart, 1997).
21. A. Kurganov, S. Noelle, and G. Petrova, Semi-discrete central-upwind schemes for hyperbolic conservation laws and Hamilton–Jacobi equations, *SIAM J. Sci. Comput.* **23**, 707 (2001).
22. A. Kurganov and E. Tadmor, New high-resolution central schemes for nonlinear conservation laws and convection-diffusion equations, *J. Comput. Phys.* **160**, 241 (2000), doi:10.1006/jcph.2000.6459.
23. P. Lax, Weak solutions of nonlinear hyperbolic equations and their numerical computation, *Comm. Pure Appl. Math.* **7**, 159 (1954).
24. P. Lax, Hyperbolic systems of conservation laws, II, *Comm. Pure Appl. Math.* **10**, 537 (1957).
25. R. J. LeVeque, *Numerical Methods for Conservation Laws* (Birhäuser Verlag, Basel/Boston/New York, 1992).
26. D. Levy, G. Puppo, and G. Russo, Central WENO schemes for hyperbolic systems of conservation laws, *Math. Model. Numer. Anal.* **33**, 547 (1999).
27. K. A. Lie and S. Noelle, An improved quadrature rule for the flux-computation in high-resolution nonoscillatory central difference schemes for systems of conservation laws in multidimensions submitted for publication.

28. X. D. Liu and E. Tadmor, Third order nonoscillatory central scheme for hyperbolic conservation laws, *Numer. Math.* **79**, 397 (1998).
29. C. D. Munz, A tracking method for gas flow into vacuum based on the vacuum Riemann problem, *Math. Method. Appl. Sci.* **17**, 597 (1994).
30. H. Nessyahu and E. Tadmor, Non-oscillatory central differencing for hyperbolic conservation laws, *J. Comput. Phys.* **87**, 408 (1990).
31. S. Noelle, M. Rumpf, and W. Rosenbaum, An adaptive staggered grid scheme for conservation laws, in *Proc. Eighth Int. Conf. Hyp.Problems, Magdeburg 2000*, edited by Freistühler and Warnecke, in press.
32. Y. Nohguchi, K. Hutter, and S. B. Savage, Similarity solutions for granular avalanches of finite mass with variable bed friction, *Continuum Mech. Thermodyn.* **1**, 239 (1989).
33. S. B. Savage and K. Hutter, The motion of a finite mass of granular material down a rough incline, *J. Fluid. Mech.* **199**, 177 (1989).
34. S. B. Savage and K. Hutter, The dynamics of granular materials from initiation to runout. Part I: Analysis, *Acta. Mech.* **86**, 201 (1991).
35. S. B. Savage and Y. Nohguchi, Similarity solutions for avalanches of granular materials down curved beds, *Acta. Mech.* **75**, 153 (1988).
36. Y. C. Tai, *Dynamics of Granular Avalanches and Their Simulations with Shock-Capturing and Front-Tracking Numerical Schemes*, Doctoral Dissertation (Darmstadt University of Technology, Germany, 2000).
37. Y. C. Tai and J. M. N. T. Gray, Limiting stress states in granular avalanches, *Ann. Glaciol.* **26**, 272 (1998).
38. Y. C. Tai, S. Noelle, J. M. N. T. Gray, and K. Hutter, An accurate shock-capturing finite difference methods to solve the Savage–Hutter equations in avalanche dynamics, *Ann. Glaciol.* **32**, 263 (2001).
39. E. F. Toro, *Riemann Solvers and Numerical Methods for Fluid Dynamics*, 2nd ed. (Springer-Verlag, New York/Berlin/Heidelberg, 1999).
40. B. Van Leer, Towards the ultimate conservative difference scheme V, *J. Comput. Phys.* **32**, 101 (1979).
41. M. Wieland, J. M. N. T. Gray, and K. Hutter, Channelized free surface flow of cohesionless granular avalanches in a chute with shallow lateral curvature, *J. Fluid Mech.* **392**, 73 (1999).
42. H. C. Yee, Construction of explicit and implicit symmetric TVD schemes and their applications, *J. Comput. Phys.* **68**, 151 (1987).